

# A Human-Scale Clinically Ready Electromagnetic Navigation System for Magnetically Responsive Biomaterials and Medical Devices

Simone Gervasoni,\* Norman Pedrini, Tarik Rifai, Cedric Fischer, Fabian C. Landers, Michael Mattmann, Roland Dreyfus, Silvia Viviani, Andrea Veciana, Enea Masina, Buse Aktas, Josep Puigmartí-Luis, Christophe Chautems, Salvador Pané,\* Quentin Boehler, Philipp Gruber, and Bradley J. Nelson\*

This paper is dedicated to the memory of Tarik Rifai, who passed away in June 2019 at an early stage of this work


Magnetic navigation systems are used to precisely manipulate magnetically responsive materials enabling the realization of new minimally invasive procedures using magnetic medical devices. Their widespread applicability has been constrained by high infrastructure demands and costs. The study reports on a portable electromagnetic navigation system, the Navion, which is capable of generating a large magnetic field over a large workspace. The system is easy to install in hospital operating rooms and transportable through health care facilities, aiding in the widespread adoption of magnetically responsive medical devices. First, the design and implementation approach for the system are introduced and its performance is characterized. Next, *in vitro* navigation of different microrobot structures is demonstrated using magnetic field gradients and rotating magnetic fields. Spherical permanent magnets, electroplated cylindrical microrobots, microparticle swarms, and magnetic composite bacteria-inspired helical structures are investigated. The navigation of magnetic catheters is also demonstrated in two challenging endovascular tasks: 1) an angiography procedure and 2) deep navigation within the circle of Willis. Catheter navigation is demonstrated in a porcine model *in vivo* to perform an angiography under magnetic guidance.

## 1. Introduction

Over the past two decades, significant progress has been made in magnetic micro- and nanomaterials for applications in health care, ranging from nanoparticles, nanowires, and composites, to more sophisticated assemblies and architectures, such as magnetic microrobots and microcatheters.<sup>[1–3]</sup> These small-scale devices hold significant potential in minimally invasive medicine, especially for targeted drug delivery and cell manipulation.<sup>[4–6]</sup> The key principle involves leveraging the ability of these materials to navigate within biological fluids, tissues, and confined areas within the human body using externally generated magnetic fields.<sup>[7–9]</sup>

The advantage of magnetism over other navigation approaches, such as light or ultrasound, is that the body is essentially transparent to magnetic fields. These fields are biocompatible across various

S. Gervasoni, N. Pedrini, T. Rifai, C. Fischer, F. C. Landers, M. Mattmann, R. Dreyfus, S. Viviani, A. Veciana, E. Masina, B. Aktas, C. Chautems, S. Pané, Q. Boehler, B. J. Nelson  
 Multi-Scale Robotics Lab  
 ETH Zurich  
 CH-8092 Zurich, Switzerland  
 E-mail: [gesimone@ethz.ch](mailto:gesimone@ethz.ch); [vidalp@ethz.ch](mailto:vidalp@ethz.ch); [bnelson@ethz.ch](mailto:bnelson@ethz.ch)

 The ORCID identification number(s) for the author(s) of this article can be found under <https://doi.org/10.1002/adma.202310701>

© 2024 The Author(s). Advanced Materials published by Wiley-VCH GmbH. This is an open access article under the terms of the [Creative Commons Attribution-NonCommercial-NoDerivs](https://creativecommons.org/licenses/by-nc-nd/4.0/) License, which permits use and distribution in any medium, provided the original work is properly cited, the use is non-commercial and no modifications or adaptations are made.

DOI: 10.1002/adma.202310701

J. Puigmartí-Luis  
 Departament de Ciència dels Materials i Química Física  
 Institut de Química Teòrica i Computacional, University of Barcelona (UB)  
 08028 Barcelona, Spain

J. Puigmartí-Luis  
 Institució Catalana de Recerca i Estudis Avançats (ICREA)  
 Pg. Lluís Companys 23, 08010 Barcelona, Spain

P. Gruber  
 Kantonsspital Aarau AG  
 Tellstrasse 25, CH-5001 Aarau, Switzerland

frequencies and strengths, and offer diverse ways to propel small-scale devices. Their motion mechanisms can be tailored by designing an appropriate magnetic architecture and applying suitable magnetic inputs, such as field gradients or rotational fields.<sup>[10–15]</sup> Magnetic navigation's remote manipulation capabilities hold substantial benefits for procedures such as neurovascular and endocardial interventions. By operating directly within the vasculature, craniotomies and open-heart surgeries can often be avoided, reducing the risk for patients. This approach is especially appealing for compliant tools, such as flexible catheters, endoscopes, and untethered robots, across different sizes and applications. The use of flexible instruments lessens the risk of internal lesions<sup>[16–18]</sup> and perforations while offering superior functionality compared to rigid counterparts. Furthermore, magnetic navigation enables remote procedures, minimizing medical personnel's exposure to ionizing radiation hazards. Among these hazards, fluoroscopy contributes the most to the annual radiation dose in medical settings.<sup>[19–23]</sup>

Despite substantial advancements in magnetic tools, significant hurdles exist in effectively transitioning these devices into clinical applications. A main challenge is the realization of a MNS that allows actuation of diverse magnetic devices at different scales, while also being compatible with health care facilities and imaging equipment, such as CT scanners and fluoroscopes. An MNS consists of magnets located around the body of the patient. These are either permanent magnets, which are rotated and/or translated in order to modulate the generated magnetic field, or electromagnets in which the magnetic fields are regulated by the amount of electrical current that circulates through conductive windings. The only three commercial MNS that have transitioned to the operating theater are from Stereotaxis Inc., Magnetecs, and Aeon Scientific AG. Stereotaxis' systems have performed over 100 000 procedures to date,<sup>[24]</sup> with 123 Niobe units installed worldwide as of 2019.<sup>[25]</sup> All three systems are large and heavy, and demand extensive hospital infrastructure, which poses challenges for many health care institutions.

These systems are not designed for generating magnetic field gradients or rotating magnetic fields, limiting their utility to specific tasks, such as manipulating magnetic tools for selected procedures, such as electrophysiology studies or endocardial ablation. Stereotaxis' dependence on permanent magnets prevents the deactivation of the generated magnetic fields, thus constantly posing risks including the unintended attraction of tools, interference with nearby equipment, and the creation of magnetic fields surpassing regulatory limits. These hurdles underscore the need for strategies to enhance the feasibility and safety of magnetic navigation within medical settings. Recent electromagnetic navigation systems have been proposed<sup>[26,27]</sup> to address some of the current limitations. While these systems represent a significant improvement over previous setups, they do not fulfill all requirements for a clinical setting. The main limitation of these systems is that they significantly restrict the available imaging modalities, for example, the range of angles achievable by the fluoroscope. These limitations are often linked to the system's geometry, which affects the fluoroscope's image view. Additionally, the easy integration of the MNS

into an operating room is important. Modern operating rooms house a multitude of equipment, and any newly introduced system must be compatible while imposing minimal infrastructure requirements.

Understanding the present capabilities of magnetic navigation technologies and their future prospects will aid specialized researchers engaged in the engineering of small-scale magnetic devices, especially those focused on the fabrication and design of magnetic materials. This entails understanding the range of magnetic fields that can be effectively applied, as well as the anticipated operational forces and torques within realistic workspaces, such as the human head, abdomen, and extremities. Both magnetic force and torque depend on the material's magnetization at a given applied magnetic field. By considering these aspects and the limitations and capabilities of realistic magnetic navigation systems, researchers can align their efforts more effectively, optimizing the design and functionality of tiny magnetic devices.

We present an advanced electromagnetic navigation system (eMNS), the Navion (**Figure 1**). The system is portable and tailored for magnetically-assisted minimally invasive surgery. Navion is designed to seamlessly integrate into clinical workflows as a self-contained mobile unit. The system is built upon a mobile platform that incorporates all necessary subsystems for generating magnetic fields in diverse spatial directions. With a weight of ~400 kg, it can generate a magnetic field ranging between 5 and 50 mT. The workspace spans up to 400 mm from the surface of the electromagnets. Gradients of 250 mT m<sup>-1</sup> and rotating magnetic fields of up to 10 Hz are also possible. We have designed the system to be positioned at the head of the patient bed, where the electromagnets align with the patient's head. Navion utilizes a triangular arrangement of three high-current electromagnets, creating a plane that accommodates a ceiling-mounted monoplanar fluoroscope C-arm. This arrangement preserves fluoroscope image quality in various orientations, which is particularly advantageous for neurovascular procedures requiring this imaging approach. We initially demonstrate the manipulation of small-scale robotic structures, such as spherical hard-magnetic robots, walking tubular soft-magnetic robots, particle swarms, and hard-magnetic artificial bacteria flagella (ABFs). Untethered magnetic-responsive structures are promising candidates for future minimally invasive procedures. The system's capabilities are subsequently demonstrated using both conventional and custom-made catheters in a controlled in vitro setting using a silicone model mimicking the human neurovasculature. The custom catheter is based on a custom hydrogel-coated distal tip. Finally, operating room (OR) integration-validation is carried out in an in vivo porcine model, showcasing the system's performance and potential for practical applications.

While we showcase a single unit, the system offers the flexibility to integrate supplementary modular assemblies of electromagnetic systems including additional Navions. This feature has the potential to amplify the magnetic forces and torques that can be applied within practical working environments. We envision that this system will facilitate the full realization of magnetic micro- and nanorobotic platforms for treating a number of conditions in the near future.



**Figure 1.** Schematic illustration of a magnetically guided neurovascular procedure using Navion and a fluoroscope in a clinical setting. In this configuration, A) Navion is placed at the head of the fluoroscope bed. The fluoroscope approaches the OR bed from the side and is able to move and rotate in the space around the patient. B) A variety of magnetic structures can be used in conjunction with Navion spanning from traditional tethered devices such as magnetic catheters to future untethered medical devices such as magnetic microrobots. C–E) Detail of the yoke coil unit on the Navion system from the outside cover to the magnetic field generated in space. F) Isosurfaces of maximum magnetic field magnitudes achievable in front of the yoke coil unit.

## 2. Results

### 2.1. Electromagnet Design for Navion

In remote magnetic navigation (RMN), an eMNS generates magnetic fields that induce a magnetic force  $\mathbf{F}$  and a magnetic torque  $\mathbf{T}$  on magnetically responsive components embedded in the tool<sup>[28]</sup> to be steered as

$$\mathbf{F} = (\mathbf{m} \cdot \nabla)\mathbf{B} \quad (1)$$

$$\mathbf{T} = \mathbf{m} \times \mathbf{B} \quad (2)$$

where  $\mathbf{m}$  is the dipole moment of the magnetic object, and  $\mathbf{B}$  the magnetic field externally generated at its position. The magnetic moment linearly increases with the volume of the magnetic

structure and its magnetization. For permanent magnets, as they are usually at remanence, the magnetization can be assumed as insensitive to the external magnetic field, while for soft-magnetic materials, the magnetization is related to the external field by the magnetic susceptibility of the material.<sup>[29]</sup> In the case of a magnetic catheter and guide wires, the magnetically responsive components are generally embodied by permanent magnets embedded in a flexible tip segment mounted at the distal end of the catheter or guide wire. The magnetic tip allows the external magnetic field to deflect the medical catheter tip, facilitating the guidance of the catheter.<sup>[30,31]</sup>

The ability to magnetically deflect the tool tip is directly related to the magnitude of the magnetic field that can be generated by the eMNS in the volume where the magnetic tool will be manipulated. The main challenge in providing a high-magnitude magnetic field, resides in the magnetic field

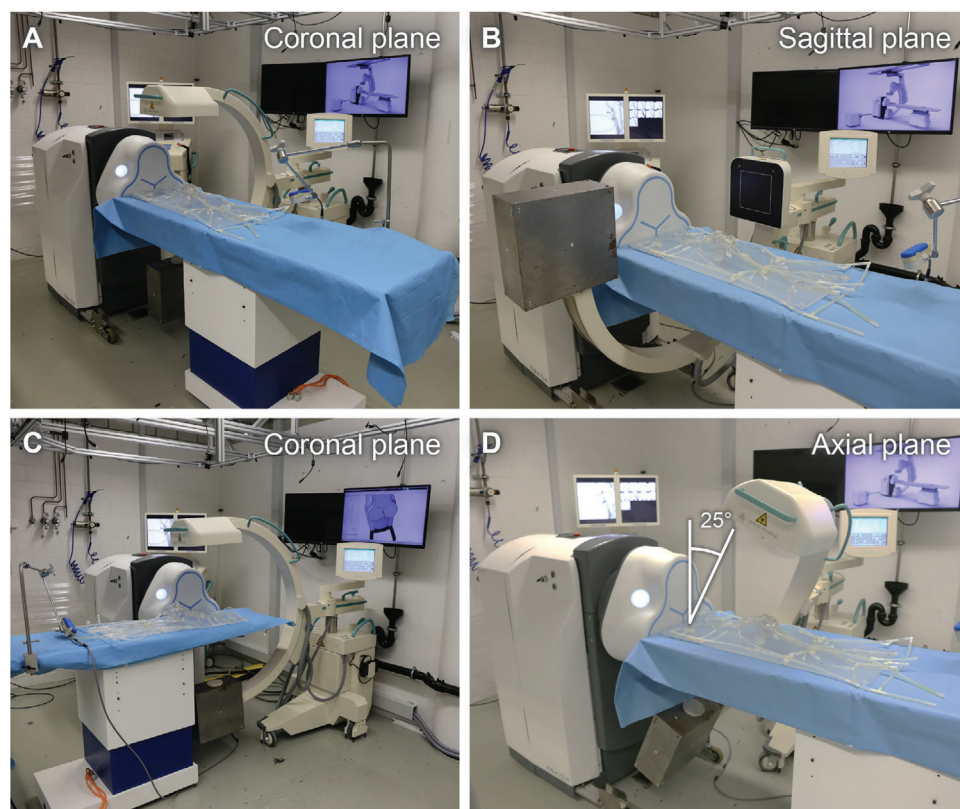


**Figure 2.** Different configurations in which the Navion system can be employed. A, B) The Navion is positioned at the head of the surgical bed allowing the fluoroscope C-arm to fully rotate around the bed. This type of configuration is suitable for neurovascular and neurosurgical procedures. The fluoroscope can continuously transition between the coronal and sagittal planes. In (C), the fluoroscope is rotated between the coronal and the axial plane, with a range of +10 to -25 degrees with respect to the fluoroscope panel starting at the coronal plane. D) The Navion is positioned on the side of the bed. The fluoroscope is capable of accessing the operating volume from two directions (bed head side and opposite of Navion). In all four configurations, the patient is accessible from both sides, thus allowing the same access to the patient as in a standard manual procedure.

magnitude decay with the cube of the distance from the field source.

If a solenoid is assumed as the field source, the magnitude  $B$  of the magnetic field produced along its main axis at a distance  $z$  from the source can be estimated using the Biot-Savart law as follows:

$$B(z) = \frac{\mu_0 I R^2 N}{2(R^2 + z^2)^{\frac{3}{2}}} \quad (3)$$

where  $\mu_0$  is the magnetic permeability of free space. Three paths can be followed to increase the magnetic field magnitude. One can decrease the electromagnet radius  $R$ , increase the number of windings  $N$ , or increase the current  $I$ . Decreasing the radius limits windings poses constraints on the maximal size of the workspace.<sup>[32]</sup> Maximizing the workspace allows the system to be used over large anatomical areas. Increasing the number of windings increases the size of the system and its footprint, limiting integration in a clinical setting. Increasing current generates more heat, increasing the thermal stress on the system, which can lead to catastrophic damage to the device if not removed accordingly. In this work, the focus was on reducing the system's footprint to favor better OR integration. To achieve this, we concentrated on increasing the current flowing in the electromagnets by ex-

ploting a custom winding technique. By increasing the current, higher magnetic fields can be achieved without increasing the electromagnet size.

Traditional electromagnets are wound around a solid core using a conductive wire. To maximize the resulting magnetic field, the windings are wound as close as possible to each other on the magnetic core. This winding strategy results in minimal gaps between the winding layers limiting the area accessible on the electromagnet to exchange the heat from the winding to a cooling fluid (Figure S1, Supporting Information). The electromagnets used on the Navion system utilize a new winding technique in which the conductive wire cross section is formed during the winding around the magnetic core. The pre-formed wire, once fully wound along the core length, forms sets of cooling channels through the entire winding pack. These extra channels allow the cooling fluid to flow through the volume of the electromagnet winding. The increased wire surface exposed to the cooling fluid allows for an increase in the heat removal from the electromagnet (Figure S1, Supporting Information). When comparing an electromagnet with standard winding to a Navion electromagnet, assuming a current of 30 A, the steady state temperature was 62 °C for the standard winding and 38 °C for the new winding strategy. When supplied with 70 A, the standard winding reached 100 °C causing the coolant to boil, while

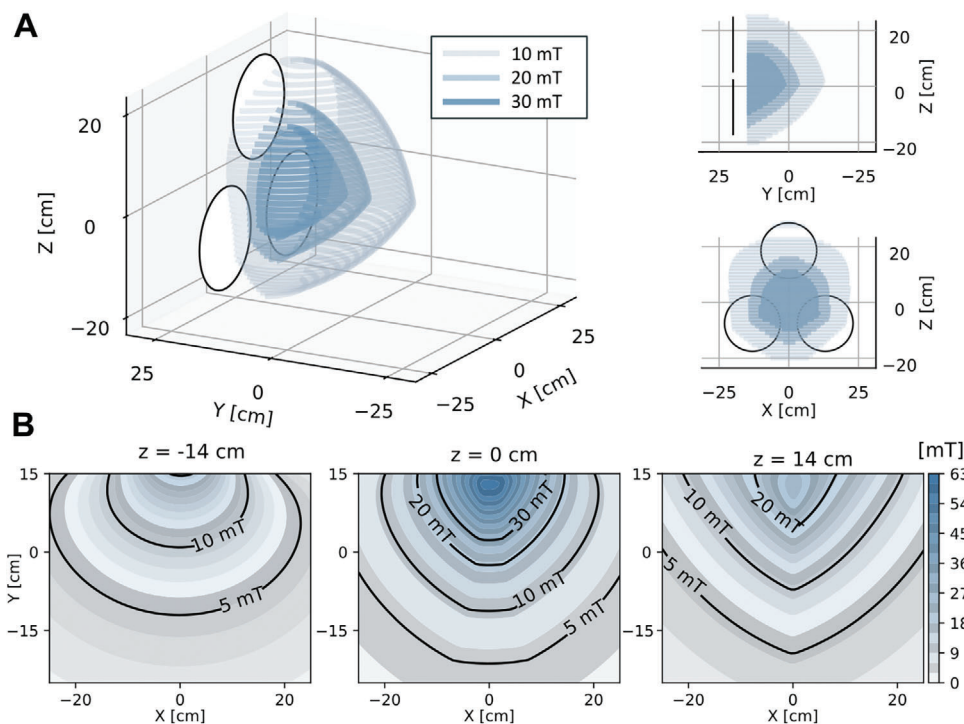


**Figure 3.** Magnetic performance of the Navion. A) Boundaries of the magnetic-feasible workspace as defined in ref. [32], for the generation of magnetic field magnitude of 10, 20, and 30 mT in any direction in space, and maximum currents of 50 A in each coil. The front of the coils are represented by the white circles. B) Maximum magnetic field magnitude achievable at three different heights.

the new winding strategy reached a steady-state temperature of 62 °C. The magnetic field difference on the surface of the electromagnets between the two winding strategies was 0.9 %. Given the same operating temperatures of the electromagnets, the new winding strategy allows for an increase in current that results in a power 5.4 times greater than the traditionally wound electromagnet.

Since the magnetic field amplitude increases with the current in the electromagnet (Equation 3), an increase in the allowable current allows for the use of smaller electromagnets while maintaining the same generated magnetic field. Each electromagnet has a diameter of 186 mm, a length of 115 mm, and can operate with a power of 10 kW.

## 2.2. Electromagnet Configuration

The Navion utilizes three electromagnets positioned in a flat triangular arrangement (Figure 1C-F). This solution was chosen to reduce the volume occupied by the system around the patient bed which could impede patient access and hinder the incorporation of a C-arm fluoroscope. The chosen arrangement results in a trade-off between magnetic performance and accessibility for other medical equipment and personnel. While electromagnets configured in a spherical geometry are optimal for magnetic field performance,<sup>[33]</sup> this arrangement must surround the patient, complicating the integration of other medical equipment. For the applications that Navion was designed for, fluoroscopy is of paramount importance. The main chal-

lenge in integrating with a fluoroscopic C-arm is the range of motion of the C-arm itself. Depending on the C-arm, rotations of up to 90 degrees are possible, for example switching between the coronal plane and the sagittal plane. To maximise the compatibility with current C-arms, lower magnetic performance was accepted to increase the achievable angles of a compatible C-arm.

With respect to the fluoroscope positioning, the planar electromagnet arrangement allows for different configurations and angles of the C-arm. Figure 2 shows four example positioning of the C-arm and the Navion system. In configurations (A) and (B), the Navion is positioned at the head of the patient bed allowing the fluoroscope C-arm to freely transition between imaging the coronal plane and the sagittal plane. In Configurations (C) and (D), the Navion is positioned at the side of the patient bed allowing the C-arm to move between the coronal plane and the axial plane. Depending on the type of minimally invasive operation either Navion position was beneficial.

## 2.3. Magnetic Field Performance

Navion is able to control the direction and amplitude of the magnetic field at any chosen position in a calibrated volume of  $40 \times 40 \times 40$  cm in front of the coils. Practical constraints, such as power consumption and maximum achievable currents in the electromagnets, limit the magnitude of the magnetic field that can be achieved at these positions. Using the approach described in ref. [32] and a linear model of the system using the approach

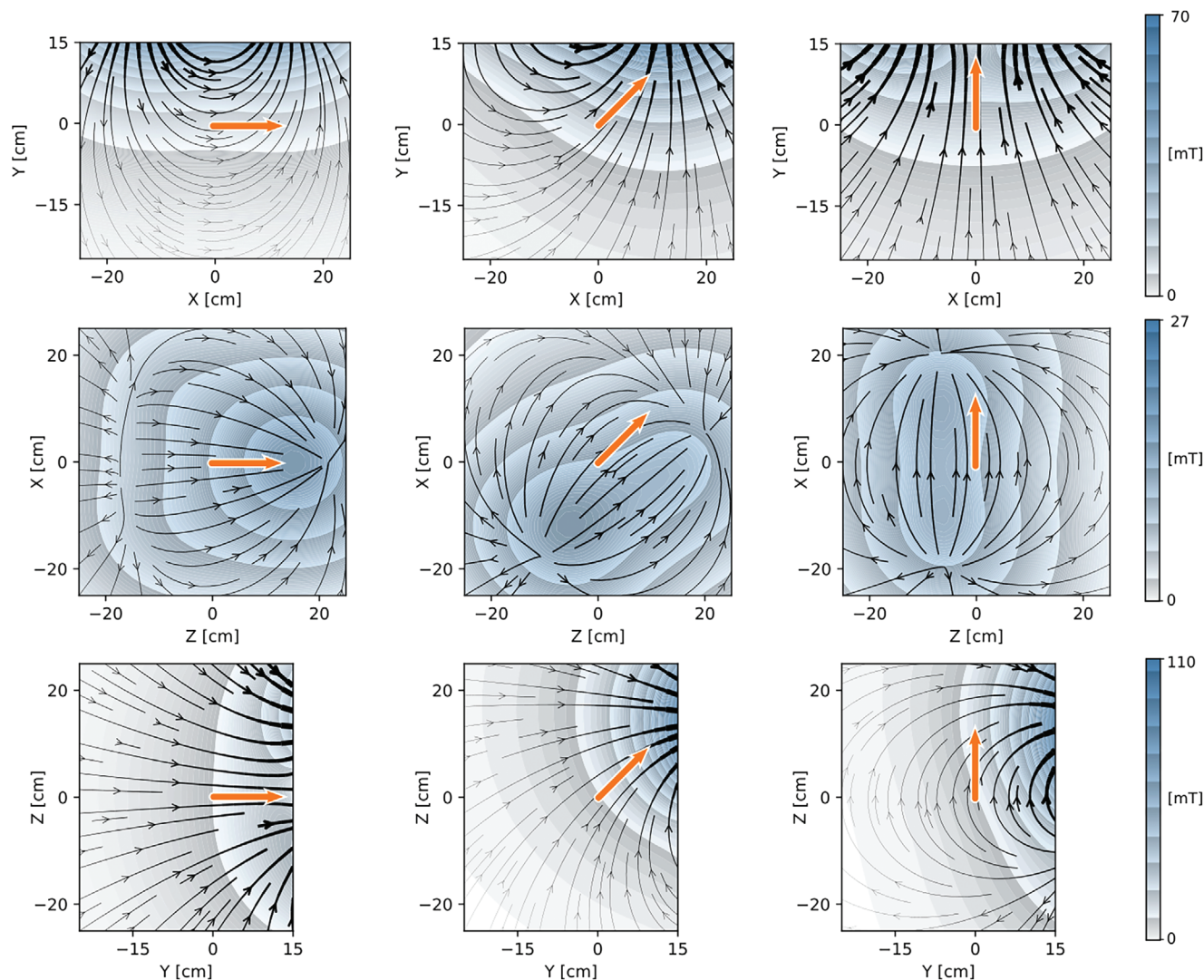


**Figure 4.** Magnetic field lines and magnetic field amplitude for different field references at 20 cm in front of the coils and at 10 mT amplitude. The desired magnetic field is depicted by the orange arrow at the center of the reference frame. The color scale represents the magnetic field magnitude.

described in ref. [34], we computed the workspace of Navion to generate a magnetic field of a desired amplitude in any direction in space. This workspace, known as the magnetic-feasible workspace, was then evaluated for different amplitudes as depicted in Figure 3A. Additionally, the magnetic performance of the system was evaluated at three different heights ( $xy$ -planes with different offsets along the  $z$ -axis, Figure 3B).

Figure 4 illustrates the magnetic field lines for different directions of the desired magnetic field specified at the center of the reference frame represented by the orange arrow. The currents in the electromagnets required to generate the desired magnetic field at the target position were computed using the inverse of the actuation matrix determined via the model of the system.<sup>[29]</sup> The actuation matrix was in turn used to evaluate the magnetic field at the other positions in the considered plane.

The unique topological arrangement of the electromagnets enables unprecedented fluoroscope positioning and a more ac-

cessible area. The planar triangular arrangement combined with the high power density electromagnets allows for a large area of accessibility around the patient while maintaining a magnetic field magnitude and homogeneity sufficient to magnetically steer magnetically responsive biomaterials and medical devices in the human body, as demonstrated in the next sections.

#### 2.4. In Vitro Navigation of Untethered Magnetic Devices

We assessed the capabilities of the Navion to navigate untethered magnetic structures within conduits comparable in size to those of human vessels while maintaining a workspace compatible with imaging modalities and at human scales. As the Navion can generate both gradients and rotating magnetic fields, several prototypical microrobotic structures with different sizes, shapes, anisotropies and materials were tested: a hard-magnetic

millisphere (Figure 5A), two micro-tubular soft-magnetic structures, each with a distinct composition (Figure 5B,C), a hard-magnetic composite microhelix (Figure 5D), and a swarm of hard-magnetic isotropic microparticles (Figure 5E). These architectures were selected as they represent typical shapes commonly employed in the area of magnetic microrobotics. The manipulation experiments were conducted in a fluidic model that reproduces human vasculature in a large workspace. The navigation was conducted with no flow, simulating the scenario in which a balloon catheter would be used to stop or reduce the blood flow for a short time. The vascular geometry in the lower section of the model closely adheres to human anatomy, including key components such as the aortic arch, carotid artery, subclavian artery, and brachiocephalic artery. In contrast, the upper section of the model has been intentionally altered to introduce varying degrees of branch tortuosity (Figure 6A). This tortuosity is visually differentiated using a color-coded scheme: blue represents easy, red signifies medium, and black indicates hard levels of tortuosity. In the context of our navigation technique, two control strategies were used. The spherical permanent magnet was navigated using pulsed gradients, while the two tubular structures, the particle swarm, and the artificial bacteria flagella (ABF) were maneuvered using rotating magnetic fields (Figure 5F).

#### 2.4.1. Navigation of a Spherical Permanent Magnet

Spherical microrobots have been proposed as embolic agents or targeted drug delivery agents. We evaluated the motion of a commercially available hard-magnetic sphere of 2 mm in diameter made of a gold-coated neodymium-iron-boron using pulsed magnetic field gradients. The spherical robot was initially positioned at the entry point of the aortic arch, simulating its delivery via a catheter through the standard femoral-to-aorta access commonly employed in neurovascular procedures. From this initial location (Video S1: 22 s, Supporting Information), the robot was steered using pulsed magnetic gradients to navigate through the model vasculature. In the first demonstration, the spherical robot was guided from the end of the aorta toward the brachiocephalic artery by generating a gradient aligned parallel with the fluidic model's long axis (Video S1: 34 s, Supporting Information). The robot was subsequently navigated into the common carotid artery. A gradient pointing to the left was then generated to allow the spherical robot to hop towards the left of the model. The magnetic field gradient was then rotated so that the spherical robot was pulled into the right bifurcation (Video S1: 69 s, Supporting Information). A combination of right, straight, and left gradients was then employed to navigate through the S-shaped features (Video S1: 80 s, Supporting Information). Finally, a magnetic gradient aligned similarly to the initial one was used to move the spherical robot towards the goal marked with a black dot at the end of the model. In the second demonstration, the spherical robot began on the right side of the aorta, just before the aortic arch. Using a combination of straight and left gradients, the sphere was directed into the left common carotid artery (Video S2: 29 s, Supporting Information). A right-pointing gradient was applied to enter the right branch at the bifurcation (Video S2: 38 s, Supporting Information). After entering the right

branch, a sequence of right, straight, right, left, and straight gradients was used to navigate the spherical robot toward a target marked with a red dot (Video S2: 45 s, Supporting Information). The magnetic gradients used in these demonstrations were  $\sim 200$  mT m<sup>-1</sup>.

#### 2.4.2. Navigation of Electroplated Cylindrical Microrobots

Magnetic tubular meso- and microstructures have emerged as promising candidates for microrobotic drug delivery. This shape is not only appealing for magnetic actuation close to surfaces, but also for functional purposes as their internal and external surfaces can integrate various compounds such as drugs or cells. Here, we navigated two compositionally distinct cylindrical structures using a rotating magnetic field generated by the Navion system. The structures are made of cobalt-nickel (CoNi) alloys (Figure S2, Supporting Information). In the first demonstration, we manipulated a commercially available Ni-rich microtube. The navigation started on the right side of the aortic arch, as if the device had been deployed in the aorta by a catheter (Video S3: 22 s, Supporting Information). Next, a counter clock-wise (CCW) in-plane rotating magnetic field of 5 mT and a frequency of 2 Hz was applied. The cylindrical robot initially moved toward the left side of the aorta until it contacted the aorta walls. Upon establishing contact, the robot followed the aorta wall in an upward direction, progressing towards the carotid artery (Video S3: 37 s, Supporting Information). To navigate the cylindrical robot into the anatomical space between the brachiocephalic artery and the left carotid artery, we tilted the axis of rotation from a vertical orientation to a 20-degree angle (Video S3: 44 s, Supporting Information). From this intermediate position, we guided the robot towards the right subclavian artery by inclining the rotating field axis 20 degrees to the left (Video S3: 55 s, Supporting Information). We then reversed the direction of the rotating magnetic field to a clockwise (CW) rotation, enabling the robot to traverse the right internal carotid artery (ICA) until it reached the bifurcation. The rotating magnetic field vector was further tilted 20 degrees to the right, facilitating the navigation of the tube through the right bifurcation (Video S3: 72 s, Supporting Information). Subsequently, we continued to guide the cylindrical microrobot until it reached the end of the branch, using an in-plane magnetic field. The average speed of this navigation process was approximately 3.5 mm s<sup>-1</sup>. In a second demonstration, we used a custom-made electroformed Co-rich CoNi microtube.<sup>[35]</sup> Similarly, we began the navigation in the aorta (Figure 6B). A CW in-plane rotating magnetic field of 5 mT at a frequency of 1 Hz was used to navigate the cylindrical robot toward the left subclavian along the aorta wall (Video S4: 31 s, Supporting Information). Upon entering the left subclavian artery, the rotation of the magnetic field was ceased, and then reversed into a counterclockwise (CCW) rotation (Video S4: 59 s, Supporting Information). This reversal allowed us to navigate the cylindrical robot through the left bifurcation and beyond, extending past the second bifurcation (Video S4: 98 s, Supporting Information). Halfway along the branch, we pivoted the rotating magnetic field by 90 degrees, aligning the rotation vector parallel to the model plane (Video S4: 110 s, Supporting Information). To return the cylindrical robot to the bifurcation, we employed an out-of-plane walking

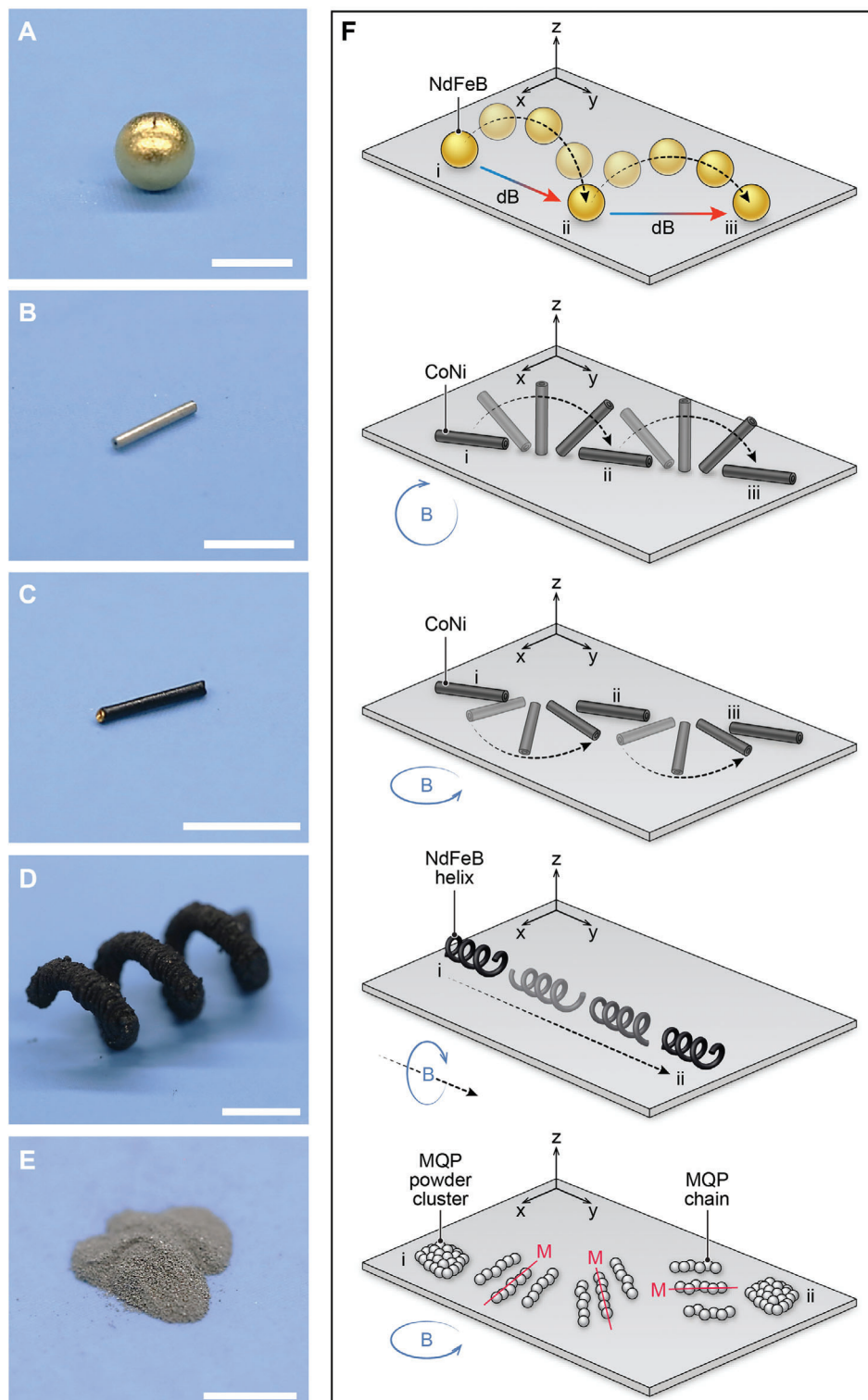


**Figure 5.** In vitro demonstration of untethered devices navigation. A) NdFeB gold coated spherical magnet with a 2mm diameter and a 1.17T bulk remanence (Scale bar 2 mm). B) Tubular structure realised by electroplating (Scale bar 3 mm), C) Tubular structure realised by electroplating (Scale bar 4 mm), D) FDM 3D printed ABF (Scale bar 8 mm). E) MQP-S-11-9-20001 powder (Scale bar 2 mm). F) Five modalities of locomotion were investigated in the demonstration. The gold spherical magnet is guided forward with pulses of the magnetic field gradient. The Nicoloy and CoNi tubes are navigated with in-plane and out-of-plane rotating magnetic fields. The NdFeB Helix ABF is navigated with a magnetic rotating field along the ABF long axis. The MQP powder is navigated with in-plane rotating magnetic fields. Unique to the MQP powder, linear structures are formed by the particles aligning under the external magnetic field. The formed lines rotated and created a swarm of lines that rotate and move together in the external rotating field.



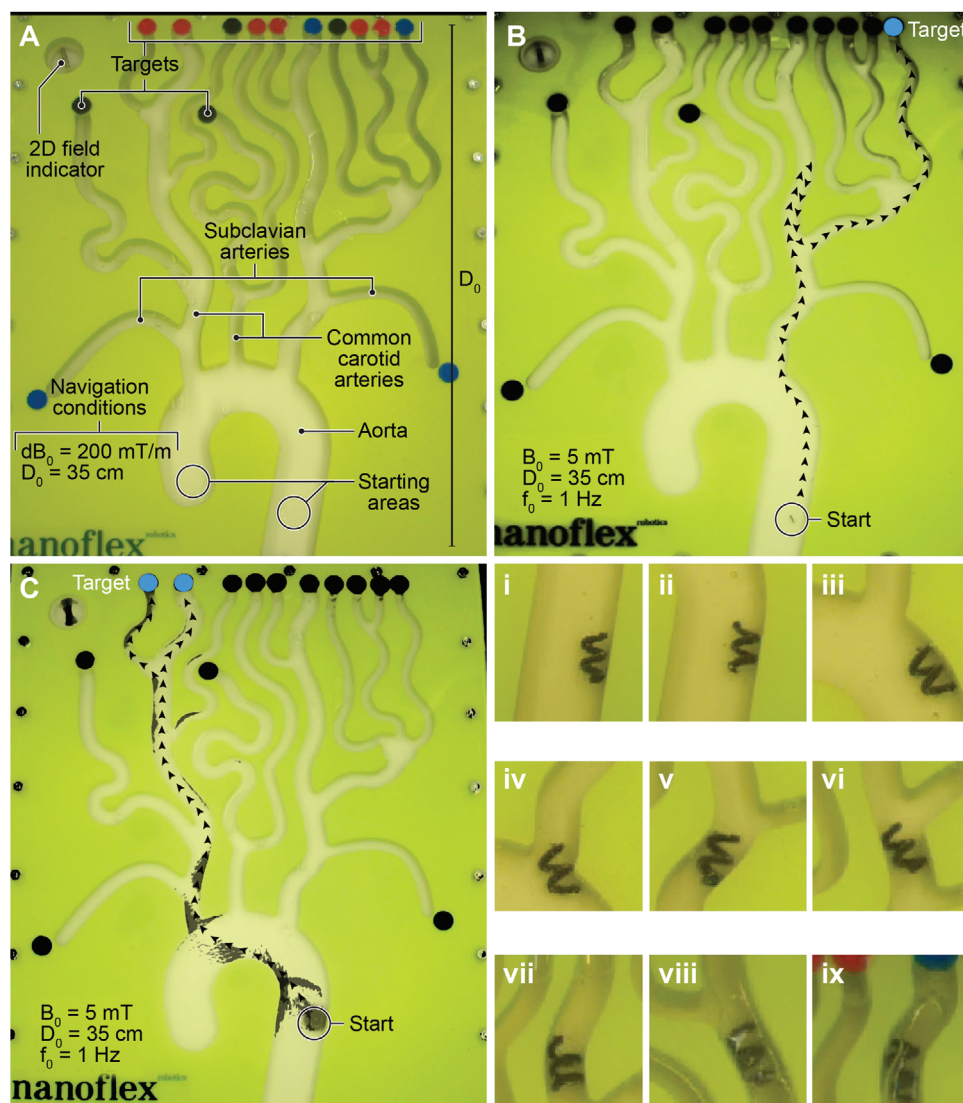


**Figure 6.** In vitro demonstration of untethered devices navigation. A) Annotated setup for magnetic structures navigation. B) Navigation of the tubular structure using rotating magnetic fields with a 1 Hz frequency and 5 mT field. The model height  $D_0$  is 35 cm and 26 cm in width. The channels have a 6 mm depth. The navigation image is obtained by superimposing 15 images with reduced opacity of the model during navigation. A combination of in-plane and out-of-plane rotating fields are used to navigate the tubular robot in the topmost left target vascular branch. C) Swarm navigation of MQP-S-11-9-20001 particles. The navigation image is obtained by superimposing 10 images with reduced opacity of the model during the navigation. The particles are navigated using a combination of in-plane rotating fields with the rotation vector declinated by 20 degrees with respect to in-plane normal, to determine the direction of movement. As an example, to move the swarm to the left of the image the rotation vector is declinated 20 degrees to the left from the vasculature model plane normal. D, i–ix) Sequence of the ABF navigation. The navigation is a combination of fluid propulsion and model wall interaction.

motion. At the bifurcation, the rotating magnetic field vector was once again adjusted to an out-of-plane orientation, guiding the cylindrical robot into the right branch (Video S4: 117 s, Supporting Information). The robot was then rolled along this branch until it reached the designated blue target (Video S4: 130s). The average navigation speed during this phase was  $\sim 5.6 \text{ mm s}^{-1}$ . Note that the Co-rich device could be maneuvered at 1 Hz in contrast with the Ni-rich, which displayed a slightly lower speed and required 2 Hz. Below this frequency, the Ni-rich device wobbles.

#### 2.4.3. Navigation of a Particle Swarm

Magnetic swarms have recently been investigated as potential microbotic platforms for biomedical applications. The swarms have the ability to reconfigure their shape as a function of the applied magnetic input. The swarm model used in this demonstration comprises hard-magnetic microparticles with an average size of  $50 \mu\text{m}$ . The starting point for the swarm navigation is at the entry of the aortic arch, simulating a deployment of the swarm via a catheter (Figure 6C). A magnetic field rotating CCW at 1 Hz

5 mT in the plane of the vascular model was then generated, and the swarm started to rotate (Video S5: 37 s, Supporting Information). By actively adjusting the angle of the magnetic rotating field vector the swarm was guided towards the center of the vasculature model (Video S5: 66 s, Supporting Information). The swarm was subsequently split into two smaller swarms upon colliding against the bifurcation ridge between the left carotid artery and the left subclavian artery (Video S5: 79 s, Supporting Information). By tilting the magnetic field vector towards the top of the vasculature model the two smaller swarms were navigated forward along the left branch after the subclavian entry and on the left branch after the left carotid artery entry (Video S5: 86 s, Supporting Information). In the left branch after the subclavian entry, the swarm was navigated forward along the straight branch up to the blue target (Video S5: 119 s, Supporting Information). In the left branch after the carotid entry, the swarm accumulates in the S-shape turn. To move this swarm ahead, the vector of the rotating magnetic field was first rotated towards the left and then to the right to navigate along the wall of the branch (Video S5: 143 s, Supporting Information). The magnetic field vector was declined to the right to complete the navigation to the black target (Video S5: 154 s, Supporting Information).

In the second demonstration, the particle swarm was positioned at the entry of the aortic arch. An in-plane CW magnetic field of 5 mT rotating at 1 Hz was applied (Video S6: 33 s, Supporting Information). By declining the rotating field by 20 degrees toward the left subclavian entry, the swarm was maneuvered in that direction. At the entry to the subclavian artery, the field was again declined towards the bottom of the model, navigating the swarm back into the aortic region (Video S6: 69 s, Supporting Information). Once back at the aorta, the rotating magnetic field vector was declined toward the right subclavian artery leading the swarm toward the brachiocephalic artery (Video S6: 104 s, Supporting Information). At the entry to the brachiocephalic artery, the vector of the magnetic field was declined toward the front of the model (Video S6: 159 s, Supporting Information). The swarm was navigated along the right ICA up to the bifurcation where the magnetic field was declined toward the left upper corner of the model to navigate the particle swarm inside the left branch toward the red target (Video S6: 280 s, Supporting Information).

The influence of the magnetic field properties on the behavior of the swarm was evaluated by testing different magnetic field rotation frequencies and magnitudes. Variation of the angular velocity of the magnetic field were found only to determine the speed of the swarm. Above 3 Hz, the swarm could no longer be adequately controlled.<sup>[36]</sup> Changes in magnetic field magnitude play a role up to 5 mT, which was found to be ideal for navigating the swarm. There was no significant impact observed above 5 mT. Neither parameters seemed to improve the swarm cohesion.

#### 2.4.4. Navigation of a Magnetic Composite Helical Device

A common magnetic microrobot design is the helical swimmer, also known as an artificial bacterial flagellum (ABF), because of the ability of these devices to mimic the swimming corkscrew mechanism of flagellated microorganisms, such as *E. coli*. ABFs present interesting navigation abilities in a multitude of differ-

ent fluid viscosities. Propulsion is achieved by rotating the ABF around its longitudinal axis resulting in a net translational motion. Here, a 3D printed magnetic composite ABF was navigated inside the vasculature model (Figure 6D). A rotating magnetic field of 5 mT at a frequency of 2 Hz was applied in the direction of the longitudinal axis of the ABF. The ABF started to rotate with the same rotation frequency as the external field (Video S7: 20 s, Supporting Information). The ABF navigation started at the right side of the aorta. The ABF propelled itself along the wall of the vasculature model (Video S7: 32 s, Supporting Information). The wall of the model provided additional stability to the ABF and prevented lateral drifting. The ABF advanced to the entry of the left subclavian branch (Video S7: 38 s, Supporting Information). By readjusting the rotating field vector toward the subclavian branch, the ABF could then access it. At the next bifurcation, the ABF was navigated toward the left branch until it reached the blue target at the end of the model (Video S7: 50 s, Supporting Information). The speed of the ABF in its entire path was on average 4 mm s<sup>-1</sup> and exhibited a step out frequency above 5 Hz.

## 2.5. In Vitro Navigation of Tethered Magnetic Devices

### 2.5.1. Aortic Arch and Supra-Aortic Vessel Navigation

Dexterous and reliable navigation in the aortic arch is critical for performing digital roadmaps in neuroradiology.<sup>[37]</sup> Navigation can be challenging due to the anatomy of the supra-aortic vessels connected to the aortic arch, which are subject to various anomalies and patient variability.<sup>[38,39]</sup> The complexity of navigation is mainly due to the acute angles between the vessel origin and the aortic arch.<sup>[39]</sup> As these angles approach and surpass 90°, navigation with a standard manual catheter becomes significantly more challenging due to the inability to properly steer the tool within the supra-aortic vessel. The problem is usually addressed using multiple tools with different curved tips. However, this can result in multiple attempts to successfully perform the task, thus leading to a substantially longer procedure. Here, we demonstrate how a single magnetic catheter controlled with the Navion can navigate the aortic arch and enter all the main supra-aortic vessels.

The catheter was inserted via a 4 Fr introducer sheath into the femoral artery. The initial insertion was performed by hand to bypass the watertight seal on the introducer sheath with the flexible catheter tip. Once the flexible tip had passed through the seal, the catheter was placed inside the mechanical catheter advancer. The control of the field orientation was then carried out using a remote controller to steer the catheter. The magnetic catheter was advanced along the aorta wall to heart height with a speed of 50 mm s<sup>-1</sup>. Upon reaching the beginning of the aortic arch, the magnetic field was activated (Video S8: 16 s, Supporting Information). Initially, the magnetic field vector was orientated so that the tip of the catheter was parallel to the running tangent of the aortic arch centerline, aligning the catheter tip with the aorta inner wall surface. Aligning the tip with the wall reduces the sliding friction and prevents the catheter from adhering to the soft silicone wall. As the magnetic catheter slid along the aorta wall, the magnetic field vector was rotated by the operator to continuously align the

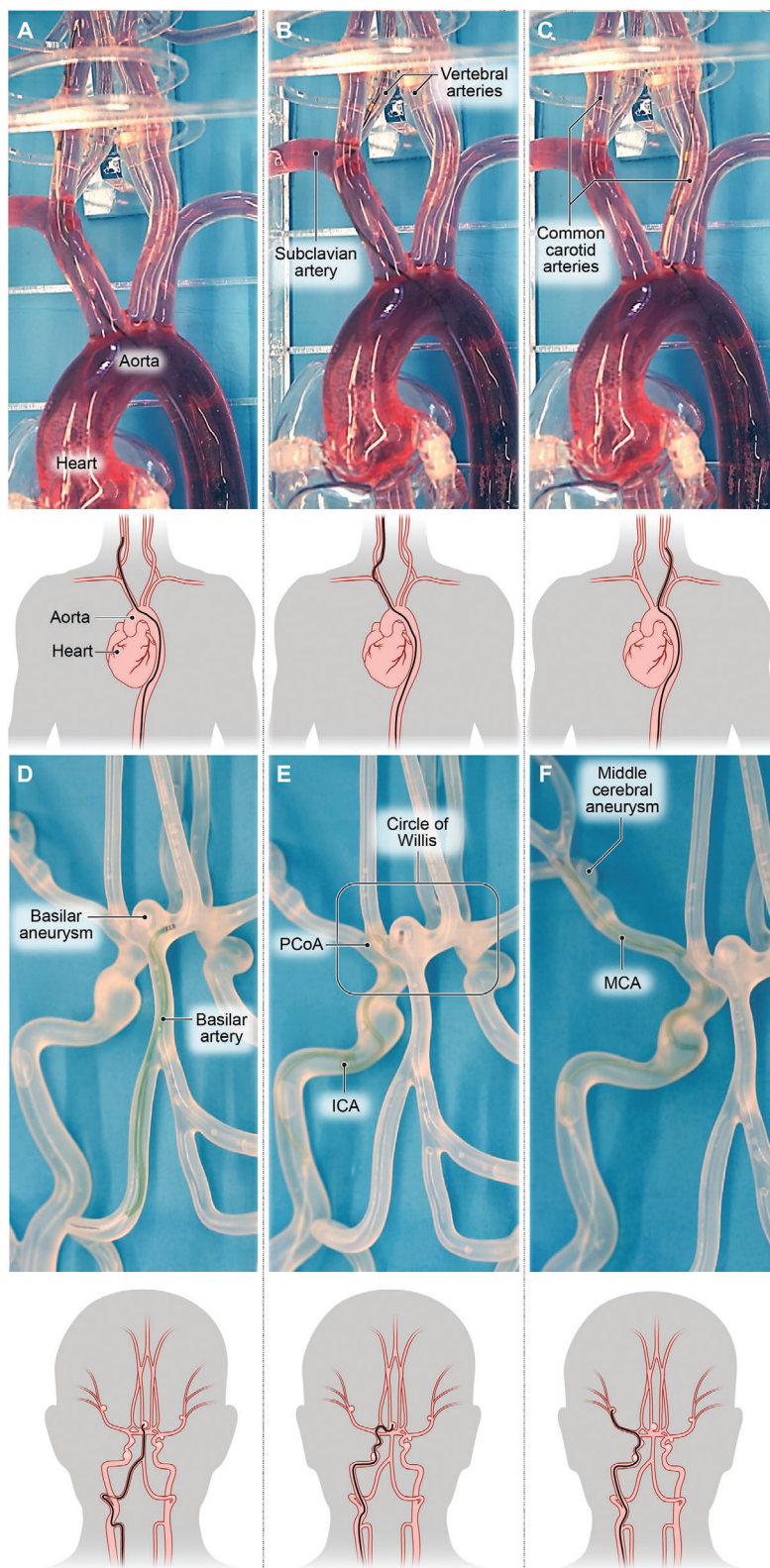


**Figure 7.** In vitro demonstration of the navigation necessary to perform a complete angiography procedure. The angiography catheter was navigated in A) the right carotid artery, B) the right vertebral artery, and C) the left carotid artery. D) in vitro demonstration of navigation tasks in the circle of Willis. The navigation of the neurovascular catheter is demonstrated starting from the vertebral artery and going through the basilar artery and into a basilar neck aneurysm, E) from the internal carotid artery through the posterior communicating artery into a basilar aneurysm, and F) from the internal carotid artery through the middle cerebral artery to a middle cerebral artery bifurcation aneurysm.

catheter tip with the wall tangent. As the catheter reached the entry to the brachiocephalic artery, the magnetic field vector was rotated to point the tip at the entry. The combination of the tilted tip, the contact with the wall, and the forward movement pushed the catheter into the brachiocephalic artery (Video S8: 19 s, Supporting Information). The magnetic catheter was then advanced through the brachiocephalic artery to the subclavian artery, the carotid artery (Figure 7A), and the vertebral artery (Figure 7B). The magnetic catheter was first navigated through the vertebral artery (Video S8: 23 s, Supporting Information), then through the carotid artery (Video S8: 29 s, Supporting Information), and finally through the right subclavian artery (Video S8: 37 s, Supporting Information). To select which entry to take from the brachiocephalic artery, the magnetic field vector was oriented to point the magnetic catheter tip towards the selected vessel (Figure 7A). The catheter was subsequently retracted back to the aortic arch. The magnetic catheter was then brought to the height of the left carotid artery (Figure 7C and Video S8: 47 s, Supporting Information). The field was projected in the direction of the carotid artery and the catheter was then advanced, as with the brachiocephalic artery. The video demonstrates the necessity to constantly adjust the direction of the magnetic field to guarantee smooth movement of the catheter inside the vessel. This is due to the softness of the artery wall model, as the tip of the magnetic catheter tends to pitch and become stuck (Figure 7B). The magnetic catheter was then retracted back into the aortic arch and aligned with the entry of the left subclavian artery. By pointing the field first towards the left vertebral artery (Video S8: 68 s, Supporting Information), then toward the subclavian artery (Video S8: 76 s, Supporting Information), the magnetic catheter was navigated through both arteries. The magnetic catheter was then fully retracted from the aorta in preparation for removal at the femoral entry point. The entire procedure was performed in less than 6 min, averaging 1 min per blood vessel insertion, using a single magnetic catheter (Figure 7C).

### 2.5.2. Navigation of Brain Arteries

The brain vasculature is an intricate network of blood vessels that can range from millimeters to micrometers in diameter, with a blood flow that can reach  $42 \text{ cm s}^{-1}$  for the larger arteries.<sup>[40,41]</sup> This network is often afflicted by life-threatening aneurysms or thrombi formation that require challenging endovascular manner navigation. Approximately 85% of aneurysms are located in the anterior circulation of the Circle of Willis,<sup>[42]</sup> which supplies blood to the brain and the surrounding structures. The circle of Willis is terminated by the basilar, vertebral, and internal carotid arteries (Figures 7D–F). The navigation of this structure and of the adjacent arteries is demanding due to the convoluted paths that the endovascular tool must travel. Here we demonstrate the ability of the Navion to steer a custom hydrogel coated magnetic catheter to reach different aneurysms and blood vessels in the vicinity of the Circle of Willis (Figure 8).

Navigation was conducted from either the beginning of the vertebral arteries or the carotid arteries. The catheter was manually inserted through a Luer–Lock valve and subsequently locked in the mechanical advancer. In this set of experiments, the mechanical advancer control strategy differs from the previous case of

aortic navigation. The rotating speed was set to the maximum level for the mechanical catheter advancer resulting in a movement that mimics the pushing movement of the neuroradiologist's hand. This rocking motion improves navigation around narrow corners of the model. In the first experiment (Figure 7D), the catheter was advanced through the common carotid artery up to the branch between the external and internal carotid arteries. In the initial step, the magnetic field was projected towards the external carotid artery, and the catheter was advanced a few centimeters into it before retracting the catheter back to the common carotid artery (Video S9: 10 s, Supporting Information). The magnetic field was then projected towards the internal carotid artery, and the catheter advanced through this to reach the Circle of Willis area. The internal carotid artery has two turns of approximately 90 deg before the branching point with the middle cerebral artery can be reached. To successfully navigate these two consecutive turns, the magnetic head of the catheter was oriented parallel to the center axis of the vessel allowing the magnetic head of the catheter to follow the natural contour of the blood vessel. In doing this, the catheter surface could freely slide along the blood vessel walls allowing the catheter to advance (Video S9: 28 s, Supporting Information), if the catheter head had not been turned, the catheter would have pinched the blood vessel walls and become stuck. Once the two turns were successfully navigated, the catheter reached the first of two aneurysms near the junction with the middle cerebral artery. At this position, the vascular model had a narrow passage of 2.1 mm OD around the first aneurysm. As the vessel diameter was comparable in size to the outer diameter of the magnetic catheter, this posed an additional challenge when aiming for the entry to this blood vessel. As shown in the video, it was necessary to advance the catheter while constantly adjusting the magnetic catheter head direction using the external magnetic field. After passing the first aneurysm, the catheter was steered into the second aneurysm (Video S9: 41 s, Supporting Information). The field was then pointed toward the middle cerebral artery (Video S9: 60 s, Supporting Information). The catheter was advanced until it reached the bifurcation for the superior and inferior trunk of the middle cerebral artery, where an additional aneurysm was present (Video S9: 73 s, Supporting Information). The catheter then returned to the common carotid artery by reversing the direction of the mechanical catheter advancer and without applying an external magnetic field.

In the second experiment, the catheter was advanced in a similar fashion to the previous experiment through the common carotid artery to the junction with the middle cerebral artery (Figure 7E). The catheter was then navigated to half the length of the middle cerebral artery (Video S10: 52 s, Supporting Information) before being reverse-navigated to the previous junction. At the junction, the catheter was then aimed towards the posterior communicating artery and advanced through it. While doing this maneuver, the catheter performed two additional 90 deg turns in addition to the two in the internal carotid artery, as previously described. These four turns were in four different planes making their navigation challenging using a normal guide wire (Video S10: 72 s, Supporting Information). At the end of the posterior communicating artery, the catheter was pointed towards the neck of the basilar aneurysm. By continuously adjusting the field while advancing the catheter in short pulses, the catheter head reached the inside of the basilar aneurysm (Video S10: 134 s, Supporting

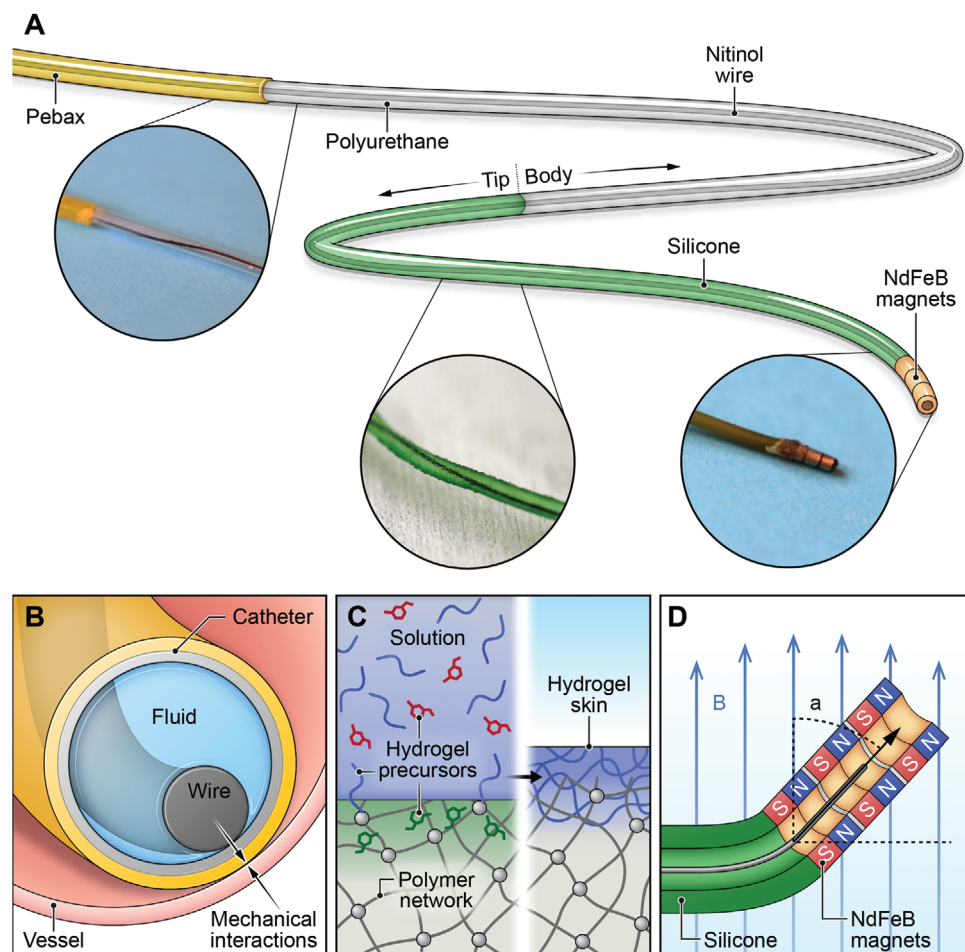


**Figure 8.** A) Neurovascular prototype catheter. The body of the catheter is composed of a Yellow Pebax body in the rear (B) and a polyurethane tube (ii) before the distal tip. To maintain buckling resistance a PTFE coated Nitinol wire is used. The Nitinol wire is smaller in diameter than the lumen inside the catheter to allow fluid to be pumped through the catheter itself. The contact with the wall surface is a combination of mechanical interactions of the Nitinol wire and the outer tubing. The distal tip of the catheter is based on a silicon tube covered with a hydrogel (C), the hydrogel is formed chemically directly on the catheter surface and confers superior lubricity to the catheter tip. The magnetic tip (D) is composed of a set of cylindrical stacked NdFeB magnets glued on the distal part of the silicon tube. When the tip is exposed to an external magnetic field  $B$ , a torque ( $a$ ) is applied to the catheter head redirecting the catheter tip.

Information). The duration of the experiment was 242 seconds. In the third experiment (Figure 7F), the catheter started from the vertebral artery where it encountered two subsequent  $90^\circ$  turns (Video S11: 16 s, Supporting Information). Navigation past these two turns was challenging due to the narrow inner diameter of the vessels of 2.7 and 3.1 mm in the narrowest segments of the second turn. After two turns, the catheter was advanced straight towards the entry to the basilar artery (Video S11: 24 s, Supporting Information). During this movement, the magnetic field was oriented parallel to the center axis of the blood vessel. Once the catheter reached the neck of the basilar aneurysm, the catheter was oriented first towards the left posterior cerebral artery (Video S11: 41 s, Supporting Information), then toward the bottom (the blue sheet) to enter the aneurysm mass (Video S11: 53 s, Supporting Information), and toward the other posterior cerebral artery (Video S11: 62 s, Supporting Information). The catheter was subsequently retracted to the beginning of the vertebral artery. The duration of the entire experiment was 55 s.

## 2.6. In Vivo Navigation of Tethered Devices in a Porcine Model

The aim of the in vivo study is to validate the safety and feasibility of using Navion for magnetically-guided neurovascular procedures. Tasks performed in vivo included roadmapping and diagnostic angiographies in the aortic arch and the neck region of a porcine model with a custom angiography magnetic catheter (Figure 9). The navigation for these different tasks did not generate vasospasms, thus showing preliminary evidence of the safety and feasibility of the approach.

The porcine model was chosen for the similarities in size and geometry of their aortic vasculature to humans.<sup>[43]</sup> The procedure began by placing the fluoroscope C-arm in the coronal plane and positioning the Navion at the head of the bed. To ensure proper placement of the Navion a 10 mm spacer was used between the Navion and the bed head. The electromagnet arrangement was raised so that the height of the center would correspond to the height of the pig's nose. After the anesthetization of the pig,

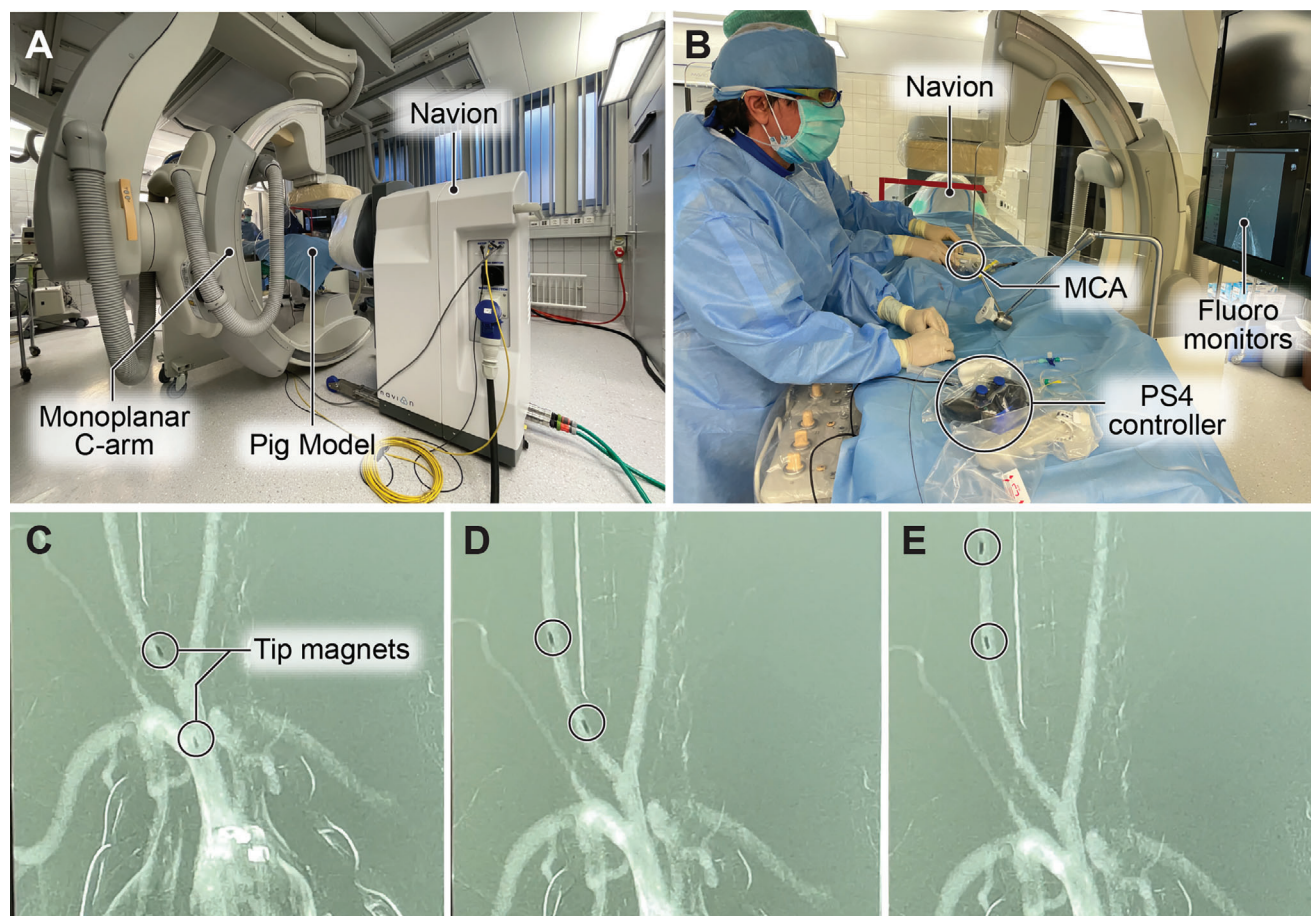


**Figure 9.** In vivo navigation of a neurovascular catheter in a porcine model. A) Navion installed in the animal lab with the fluoroscope C-arm aligned on the coronal plane. The porcine model is already on the bed below the blue surgical blanket. B) View of the operating theater in the animal lab. Navion is positioned at the bed head. The medical team operates from the left side of the porcine model. The mechanical catheter advancer was fixed using a medical arm and the fluoro-monitor was placed on the right side across the bed. The Navion controller was placed at the surgeon's discretion. C–E) Fluoroscopy view of the catheter while navigating past the porcine model aortic arch (Scale bars 10 mm).

a 4 Fr trocar was inserted into the pig's common femoral artery. Heparin was used to prevent thromboembolic events. A custom magnetically responsive angiography catheter was inserted in the trocar. The catheter was initially advanced manually by the neuro-radiologist along the pig's aortic arch. Once at the aortic arch, an initial roadmap was collected using the fluoroscope by injecting a contrast agent (Ultravist) directly through the catheter.

Following the roadmap acquisition, the Navion's magnetic field was activated and the magnetic control of the angio-catheter was started. The catheter was advanced to the innominate artery by deflecting the tip using the magnetic field generated by the Navion. A Sony PS4 Dualshock 4 controller was used by the neuro-radiologist to direct the magnetic field and advance the catheter. The neuro-radiologist used the video feed from the fluoroscope as direct feedback for the navigation. The catheter was then directed and navigated forward and backward into the right subclavian artery. From the subclavian artery, the catheter was further navigated towards the right proximal thyrocervical artery. The catheter was then retracted from the ostial part of the thyrocervical artery and slowly navigated towards the bicarotid artery reaching the middle area of the left common carotid artery. From the

common carotid artery, the catheter was retracted into the bovine arc and from there navigated into the right common carotid artery. The catheter was then navigated to the left thyrocervical artery passing the proximal aortic arc. From the left thyrocervical, the catheter was magnetically navigated into the middle of the subclavian artery and from that point to the proximal part of the left subclavian artery.

The catheter was then reverse-navigated into the aortic arch and into the bicarid artery. From the bicarid artery, the catheter was navigated into the left common carotid artery. With the distal tip of the catheter placed in the common carotid artery, a contrast agent was once more released to verify tip positioning and normal blood flow in the pig. Following the catheter tip position verification, a new projection for diagnostic angiography was established, this new projection was centered on the pig's head to create a map of the pig's brain neck and brain vasculature. Following the map acquisition, the magnetic catheter was advanced once again into the upper right common carotid artery into the proximal part of the right extracranial artery. The maxillary artery was subsequently reached by passing the 90° turn between the two. From the maxillary artery, the catheter was finally advanced

to the endpoint of the navigation in the superior labial artery. During the entire procedure, no evidence of vasospasm events or thrombi formation was encountered and no further vessel occlusion was detected.

### 3. Discussion

In comparison to existing eMNSs,<sup>[25–27,44–49]</sup> the Navion brings three core innovations to advance RMN technologies for clinical practice: 1) a new configuration of magnetic actuators, 2) high performance electromagnets, and 3) a single standalone portable design that integrates all necessary subsystems in a single mobile device. These three innovations allow Navion to provide the necessary patient accessibility while providing magnetic field magnitudes sufficient to control microrobots within the human body at clinically relevant scales to conduct complex MIS. The Navion planar triangular configuration of the electromagnets allows for the generation of magnetic fields suitable for magnetically guided neurovascular interventions while offering compatibility with fluoroscopic imaging modalities. Some configuration limitations exist if the user would like to use a biplanar fluoroscope. Depending on the degrees of freedom available in the fluoroscope articulations, certain angles and configurations are limited or not possible. This could limit the integration of Navion systems in workflows that require biplanar fluoroscopy support. The Navion geometry also allows the system to be positioned close to the patient's specific treatment area, thus enabling the use of magnetic navigation for different parts of the body with tethered as well as untethered magnetic architectures.

In the first set of experiments, we focused on the future of minimally invasive treatment, demonstrating the navigation of different meso- and micro-robots using magnetic field gradients and rotating magnetic fields. The demonstrations were conducted on a human-scale vascular model in order to show the navigation capabilities of different topological robots. Initial control of a spherical permanent magnet robot is demonstrated using gradient pulses. In this navigation mode, the currents were pulsed in the electromagnets to generate gradients in specific directions. The resulting gradient pulses generate instantaneous pulling forces on the spherical robot along the vasculature and toward the electromagnets.<sup>[50]</sup> The magnetic gradient pulses were 0.5 s in duration, and the frequency of the pulses was determined manually by the user pressing the gradient enable button on the GUI (Figure S7, Supporting Information). One limitation unique to this control strategy and not present in the other mode is the inability to push the structures away. Due to the electromagnet geometrical arrangement, the gradients generated always pull the structure towards Navion. The use of two Navions could mitigate this limitation. The cylindrical robots and the particle swarms were controlled and navigated using rotating magnetic fields. The rotating magnetic fields generated by Navion allowed full control of the different magnetic structures in every direction of the vascular model anatomy. To change the direction of the robot's trajectory, the strategy comprised declinating the vector of the magnetic rotating field about 20 degrees in the desired direction. The ability of the Navion to generate the required field on a large workspace enabled the navigation of the robot within a space of 350 mm by 260 mm. ABF navigation demonstrated that Navion is able to generate rotating fields for controlling ABFs within the

Navion workspace. Navigation of an ABF can be challenging due to gravity and the interaction between the vasculature model floor and the rotating ABF. Using the wall of the model as an additional stabilizing constraint during motion proved necessary to prevent side drift of the ABF during forward motion. The ABF also presents a cutoff frequency above the 5 Hz, where the movement becomes erratic and transitions to a long-axis rotation.

The focus of our experiments was to demonstrate control of tethered devices in vitro. We navigated a custom-made three-magnet angiography catheter through the aortic arch and neighboring vessels replicating a full angiography procedure navigation.<sup>[51]</sup> The main challenge for this type of experiment was the distance between the electromagnets and the magnetic catheter tip, which can reach up to 400 mm.<sup>[44,52,53]</sup> At this distance, the field generated is between 5 and 15 mT for a total average power of 30 kW. Excluding the initial insertion, the entire procedure was conducted remotely, with the catheter being controlled through the magnetic field and the mechanical catheter advancer, allowing the operator to complete the operation from outside the OR. In comparison to the traditional manual method, this approach allows the neuroradiologist to be completely isolated from harmful ionizing radiation during procedures,<sup>[54,55]</sup> making it not only safer but also less taxing as no lead protection equipment must be worn. The aortic arch experiments previously presented were less complex when compared to an actual operation, as the feedback was visible through the model and not through X-ray images. However, we do not expect X-ray images to be a limiting factor as the manual procedure is currently performed in this manner, relying only on X-ray image feedback.<sup>[56–58]</sup> We also demonstrated navigation deep in the brain vasculature by navigating a custom-made magnetic catheter toward common aneurysm locations. The customized magnetic catheter was coated with a hydrogel to reduce friction between the catheter walls and the internal walls of the model. This was necessary in order to pass through the many sharp turns that are encountered while navigating the complex brain vasculature. After the initial insertion of the magnetic catheter through a trocar, navigation of the catheter was fully remote starting from the common carotid artery to the bifurcation in the middle cerebral artery in ~2 min. In the second experiment, the magnetic catheter was navigated from the common carotid artery to the basilar artery, bypassing the posterior communicating arteries. Using the same setup as for the second set of experiments, we also navigated the catheter from the vertebral artery to the basilar artery and into the basilar aneurysms. In all three of the second set of experiments, the main challenges were the complexity of the vasculature geometry and wall friction. In order to advance the magnetic catheter, it was necessary to precisely steer the magnetic tip of the catheter by aligning it parallel to the vessel wall. In addition, it was beneficial to advance the magnetic catheter in a step-wise fashion rather than the constant "slow push" used for angiography. The step-wise motion facilitated the magnetic catheter to better navigate sharp turns.

We demonstrated the navigation of a custom angiography catheter in vivo in a porcine model. Although the vessels navigated in the porcine model were comparatively less tortuous than the ones in the in vitro silicone model, we demonstrated that Navion can be successfully integrated in an OR and used in seamless combination with a fluoroscopic imaging modality.

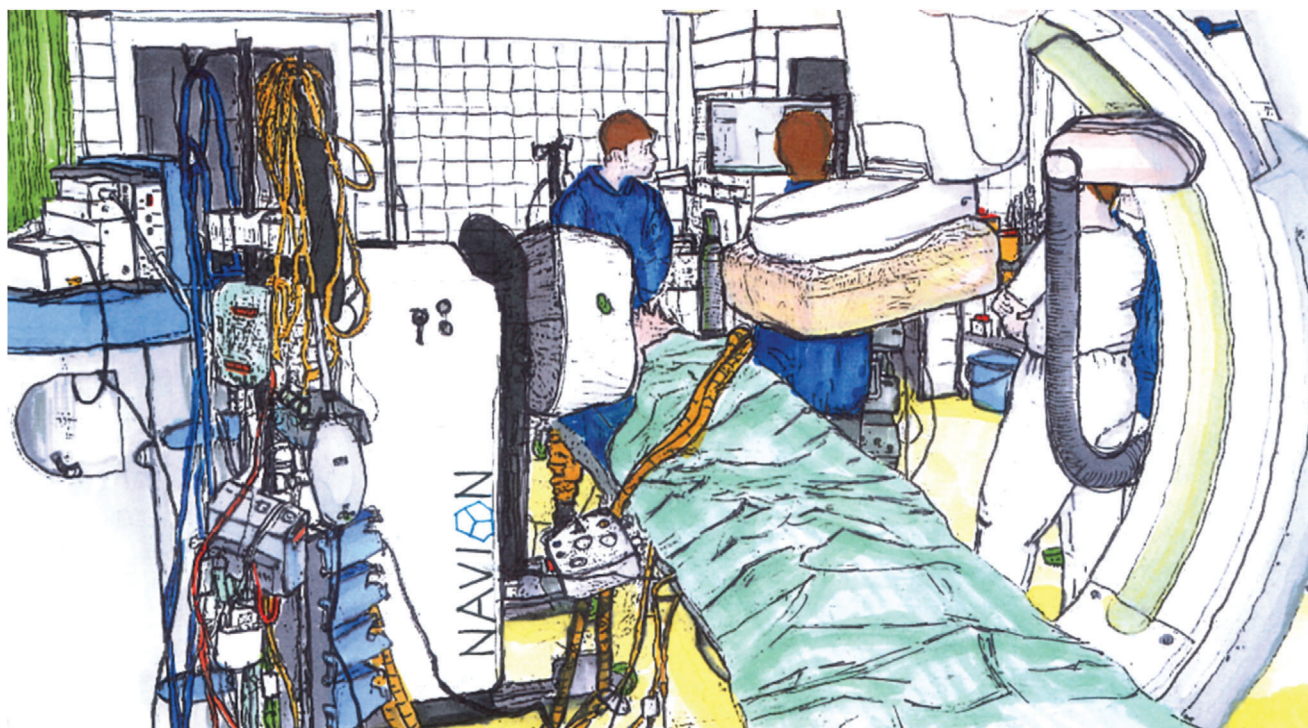


**Figure 10.** Concept image of the OR of the future. Robotic magnetic procedures are the standard of care. Navion is placed at the left of the fluoroscope bed. Navion is integrated seamlessly into the room, with the ability to position the fluoroscope to the required angles and to freely place the anaesthesia equipment around the bed. The reduced size of Navion also allows the medical personnel to freely move around the patient during the operation to address any possible challenges. The Navion can be controlled either directly from the OR using a local controller or could be remotely controlled using telesurgery.

During the animal trial, Navion was operated for 10 h continuously, demonstrating system robustness for real procedures. In these experiments, an off-the-shelf gaming controller was used with custom mapping to steer the device. Navigation interfaces for specific procedures in neuroradiology have already been developed for Navion, and have the potential to allow more efficient and intuitive interaction with the user in future procedures.<sup>[59,60]</sup>

While we demonstrated the ability of the Navion to navigate untethered microdevices *in vitro*, their *in vivo* navigation is still to be investigated for specific clinical applications and lies beyond the scope of the present paper. Additional challenges related to the design of the devices themselves are still to be addressed, such as their adequate radio-opacity for robust detection in fluoroscopic images.

In summary, Navion, with its core innovations, demonstrated that large eMNSs are not required for navigating microbots and micro guidewires and catheters at the human scale. We believe that Navion possesses many necessary features for the successful translation and implementation of magnetically tethered and untethered devices for future medical procedures (Figure 10). The future use of Navion in clinical settings will provide better protection for the medical personnel *in situ* from ionising radiations generated by fluoroscopes, and paves the way for a wider adoption of precision telesurgery for emergency procedures performed from expert centers, such as mechanical thrombectomies<sup>[61–63]</sup> and fetal surgeries.<sup>[64,65]</sup>

## 4. Experimental Section

### System Architecture

The electromagnets and the related hardware were all contained inside a wheeled cart. The cart has a footprint of 620

870 mm. The total weight of Navion was 400 kg and it had four 200 mm diameter wheels. The system height was 1250 mm in total, and the electromagnet arrangement was adjustable in height and offered a 250 mm elevation change to adapt to different heights of operating bed. Navion required a 3-Phase 63 A plug and access to water as room installation requisites. Key specifications of the system are provided in Table S5 (Supporting Information).

The system was equipped with an industrial-embedded computer that handles all low-level logic, including sensor signal conditioning and electromagnet drivers. The system was externally controlled via a control computer that communicates with the embedded computer so that different control input devices and graphical user interfaces could be used depending on the requirement of each specific procedure.

Given the high energy density of the electromagnets, liquid cooling was required to remove the Joule heat generated by the coil windings. Navion utilized a submerged liquid–solid convection cooling system, where the coolant was in direct contact with the electromagnet windings (Figure S1, Supporting Information). To guarantee electrical isolation and low viscosity, a perfluoroether oil was chosen as the cooling medium. This had a dielectric strength range superior to 25 kV (0.254 mm gap) and a viscosity of  $0.71 \text{ mm}^2 \text{ s}^{-1}$ . The three electromagnets were connected in a star pattern, where the inlet and outlet of each electromagnet cooling loop joined their respective common manifolds at the center rear of a yoke plate. The inlet manifold was directly connected to a turbine pump, while the outlet



manifold is connected to a heat exchanger hot input side. To compensate for the heat expansion of the coolant in the primary loop, an expansion vessel was connected immediately after the heat exchanger hot-side inlet. The expansion vessel also doubled as a filling unit and coolant reservoir. The hot coolant coming from the manifold outlet was then passed through a plate heat exchanger before returning to the pump. In the plate heat exchanger, the perfluoroether oil transferred the absorbed heat through the secondary cooling loop. The secondary cooling loop inlet and outlet were directly connected to a water tap and a water drain. While operating at full power, the system utilized 30 L of water per minute to cool the secondary loop. The secondary cooling could also be operated in a closed-loop manner, utilizing, for example, a pre-existing internal hospital cooling circuit.<sup>[66]</sup>

The electric current in each electromagnet was controlled using DC/DC motor drivers (Gold Drum HV, Elmo Motion Control), which allowed a current of up to 50 A continuous and a peak of 100 A across the inductive load composed of the coil's windings. The drives were supplied via a rectified constant voltage DC bus (Tambourine 100 AC/DC converter, Elmo Motion Control). The system was equipped with an industrial embedded computer (CX 9020 PLC, Beckhoff) that communicated with dedicated I/O terminals for interface with the sensors and actuators. The embedded computer internally communicated with electromagnet drivers using an EtherCAT fieldbus.

The embedded computer ran a customized TwinCat3 software that implements the state machine of the system. The Navion was externally controlled using a control computer running Linux OS (Ubuntu 18.04), and a Robotic Operating System (ROS) interface that communicated with the embedded computer via a TCP/IP protocol. The external computer converted the magnetic field target to the current targets using the calibrated magnetic model. The actual current to the desired current deviated by <1% in magnitude, resulting in similar errors on the generated magnetic field. The required current values were then sent via a TCP/IP protocol to the embedded computer. The graphical user interface was based on customized ROS visualization panels (Figure S7, Supporting Information). The magnetic field was input as a combination of rotation angles and field magnitude.

### System Characterization for Magnetic Structure Design

The magnetic field produced by the electromagnet was measured by a single sensor (THM1176, Metrolab) at different distances and for different current magnitudes. Using the method described by Boehler et al.,<sup>[32]</sup> maps of the available workspace were created (Figure 3). This was necessary to quantify the maximal magnitude of the generatable magnetic field without having to measure every direction in each point of the workspace. As shown in Figure 3, the minimum magnetic field that can be generated in every direction in the workspace followed a hemispherical distribution. The magnetic magnitude isolines shape changed with respect to the distance from the center of the Navion yoke. Below the center, the magnetic magnitude isolines moved toward a circular shape, and above the center of the yoke coil unit (Figure 1C–E), the magnetic magnitude isolines tend toward a triangular shape. Using the workspace plane at the center of the yoke, Navion was capable of generating 30 mT in every direction within the first 12 cm of a roughly triangular area in front of the electromagnets. The 10 mT magnetic isoline extended past 22 cm from the electromagnet surface. The 5 mT magnetic isoline extended beyond 35 cm from the electromagnets' surface. Using these isolines as a reference, it was possible to design the magnetic structures with the correct amount of magnetic material, based on the workspace size in which the magnetic structures are supposed to operate. For example, if the Nicoloy structure is taken, using the volume of 0.235 mm<sup>3</sup>, the magnetization from the hysteresis loop (Figure S3, Supporting Information) with an external 5 mT applied field, the resulting torque on the structure would be 0.015 Nm.

To link the currents input in the electromagnets and the generated magnetic fields, Navion used a multi-source spherical multipole expansion<sup>[34]</sup> to model each electromagnet. This was needed in this case as electromagnets magnetize each other's cores, and must thus be represented by

multiple magnetic dipole sources. The validity of the magnetic model was also subject to magnetic saturation effects,<sup>[67–69]</sup> as the latter used the superposition principle and provided a linear magnetic model, which did not capture this effect.<sup>[70]</sup> It was experimentally verified that the deviations of the superposition of the magnetic fields do not significantly degrade the linear magnetic model for manipulating magnetic structures.

### Experimental Setup for in Vitro Navigation of Untethered Devices

A set of experiments was conducted to assess the capabilities of the Navion for the manipulation of untethered microbotic structures (Figure 5). Four different magnetic architectures with different sizes, shapes, and materials were tested: a magnetic millisphere, two types of microtubular structures, a microhelix and magnetic microparticles. These are representative shapes commonly used in the area of microrobotics. The model used for the untethered device was 350 mm by 260 mm in base size with a total thickness of 14 mm. The channels inside the model were 8 mm deep. The model was realized by laser cutting and stacking polyoxymethylene plates. The geometry of the vasculature was based on human anatomy for the portion comprising the aortic arch, the carotid artery, the subclavian artery, and the brachiocephalic artery. The upper portion of the model was modified to provide different levels of tortuosity of the branches. The tortuosity was marked using three different colors, blue, red, and black, being respectively easy, medium, and hard. The model was filled with tap water to approximate the vessels being filled with blood. For the ABF demonstrations, the model was filled with Rapeseed oil. The spherical permanent magnet was an NdFeB magnet with a N35 grade and a bulk flux density of 1.17 T (Figure 5A). The NiColoy (NICOForm NCF-756-001) tubular structure had a soft magnetic behavior and presented magnetic saturation at 0.69 T. The robot had a total length of 3 mm and a diameter of 0.35 mm. The inner tube diameter was 150 μm (Figure 5B). The cylindrical robot depicted in Figure 5C was produced by electroforming nickel-cobalt (Figure S12B). The device presented a soft-magnetic behavior and had a saturation magnetisation of 1.53 T (Figure S3, Supporting Information). The ABF (Figure 5D) was 3D printed using an FDM printer and a custom NdFeB-PA12 filament.<sup>[71]</sup> The helix was 8 mm in diameter and 20 mm in length. The helix was magnetized along the diameter using an external 20 000 Oe magnetic field. The robot had a total length of 4 mm and a diameter of 0.35 mm. The inner tube diameter was 125 μm. The powder used for the swarm experiment (Figure 5E) was a hard-magnetic alloy powder from Magnequench (MQP-S-11-9-200001-070). The powder had an average particle size of 50 μm with a distribution between 20 and 100 μm.

### Experimental Setup for in Vitro Navigation of Tethered Devices

Navigation in the aortic arch and the supra-aortic vessels was also demonstrated with a magnetically tipped catheter. The experimental setup is depicted in Figure 7. During this procedure, a magnetic catheter was inserted from the femoral artery and navigated to the aortic arch. The magnetic catheter was guided from there in subsequent movements through the two subclavian arteries, the two common carotid arteries, and subsequent ramification. The catheter used for this application had a 1.3 mm outer diameter and featured a Pebax<sup>[72]</sup> body with a flexible tip (Figure S9A, Supporting Information). The flexible tip was composed of three cylindrical magnets connected via flexible stainless steel springs. The catheter had an inner lumen with a 0.8 mm diameter, that enabled the injection of a contrast agent used in angiography. The two distal magnets were 2 mm in length, and the proximal one was 4 mm. The flexible section containing the magnet had a total length of 80 mm and was connected to a second 25-mm-Pebax tube (shore 35D). The 25-mm tube was connected to a third 80-mm-long Pebax tube section (shore 55D), and the 80 mm Pebax section was connected to the main catheter Pebax body with a length of 1000 mm and a shore hardness of 75D. A silicone model (Neuro Vascular System, Trandomed 3D Inc.) was used to replicate the main arteries

of the human body from the groin area up to the brain, with the circle of Willis and the adjacent arteries. The model was composed of a transparent silicone vascular network model, and a programmable pump to create different flow conditions inside the model. The model was placed on a surgical bed simulating the clinical setting of Navion as depicted in Figure 1. In Figure 7, the different anatomical regions were depicted in their anteroposterior views. A customized catheter advancer was fixed with a 4-Fr trocar with a Luer-lock valve to allow access to the femoral arteries. The angiography catheter was then inserted into the trocar and coupled to the mechanical catheter advancer, to provide a linear motion of the proximal part of the tool. The vascular silicone model was filled with DI water and red dye. A Sony PlayStation 3 Move Navigation controller was used to control the advancer and the magnetic field.

In the second experiment, the catheter was navigated through the brain section of the vasculature model. The same advancer and trocar were used. The model was filled with DI water (dye-free) to improve catheter visibility in the small vessel. The catheter used in this experiment was composed of four sections (Figure 7D). The first section consisted of a distal tip formed by a silicone tube with a nominal outer diameter of 1 mm and a length of 120 mm, and three 1 x 1 mm cylindrical NdFeB magnets stacked and glued at the tip of the silicone tube. Two transversal 300 µm holes were present in the silicon tube, 1 mm behind the position of the magnets. The distal tip was connected to a second silicone tube with a diameter of 1.10 mm and a length of 170 mm. This section was then connected to a 70 mm transparent Pebax tube with a diameter of 1.3 mm and a shore hardness of 55 A. The last section consisted of a yellow 600 mm Pebax tube with a 1.3 mm diameter and a shore hardness of 75D. A 0.40 mm diameter PTFE mandrel wrapped with a 150 µm nitinol wire was used over the total length of the catheter with the exclusion of the distal tip. The combination of PTFE/nitinol proved to be a good solution to prevent buckling along the catheter body without hindering the flexibility of the catheter.<sup>[73–75]</sup> The two silicone sections were coated on the outside with a hydrogel following the method presented in ref. [76]. The hydrogel (AAm and I-2959) coating was necessary to overcome the friction between the model's inner walls and the catheter's outer surface. In addition, it also provided a bio- and mechanical-compatible surface to interact with the blood vessel walls.<sup>[77–79]</sup>

### Experimental Setup for In Vivo Navigation of Tethered Devices

The in vivo experiments were performed on a porcine model in the animal lab at the University Zurich Hospital. The room was equipped with a Phillips FD-20 ceiling-mounted fluoroscope. The Navion was positioned at the head of the operating bed, at a 10 mm distance from the bed's edge. The Navion was cooled by tap water available in the operating room using 15 mm water hoses. Due to the limitation of the hospital infrastructure, the system was operated with a maximum power of 13 kW. The Navion was controlled by the neuroradiologist using a Sony PS4 Dualshock 4 controller directly at the bedside (Figure S6, Supporting Information). The control computer was situated in the control room of the animal lab. The compatibility of the Navion with adjacent systems in the OR was tested prior to the animal experiment, with the systems in their final locations, and the electromagnets running at their maximum currents. The adjacent system's functionalities were verified by the OR medical personnel and no faulty behaviors were recorded. The catheter used in the porcine model was a custom 4 Fr angio catheter. The catheter had an outer diameter of 1.33 mm and an inner lumen with a 0.8 mm diameter. The catheter had a total length of 1259.30 mm, the construction was based on a Pebax outer jacket containing a braided mesh (Figure S9B, Supporting Information). The mesh was made using a 304 stainless steel wire with an OD of 0.06 mm. A PTFE Liner was used inside the whole catheter length (OD 0.83 mm and ID 0.80 mm). The Pebax hardness was transitioned from shore 72D down to 35D at the distal side. In the tip of the catheter, the Pebax tubing was switched to a softer 80A polyurethane sleeve. Two NdFeB magnets were used on the tip, placed respectively at 1.3 mm and 35.3 mm from the tip end. The magnets had a 1.33 mm OD, a ID 0.86 mm, and a length of 4 mm. A Luer lock was present at the catheter's far side for

easy connection. The porcine model was of medium size with a weight of 45 kg. Heparin (10 µL kg<sup>-1</sup>) was used to prevent thromboembolic events. The contrast agent used for the angiography procedure was Iopamiro 300 from the Iopamidol series from Bracco Imaging. The pig was anesthetized for the entire duration of the procedure. The vital parameters of the pig were monitored by a veterinarian team throughout the procedure, and the pig was euthanized after the procedure. The animal study was approved by the local Committee for Animal Experimental Research (Cantonal Veterinary Office Zurich, Switzerland) under license number ZH213/2019.

### Supporting Information

Supporting Information is available from the Wiley Online Library or from the author.

### Acknowledgements

The authors acknowledge funding from the European Union's Horizon 2020 research and innovation program under grant agreement 952152 (ANGIE). This work was also supported by the Swiss National Science Foundation through grant numbers 200020B\_185039, and the ERC Advanced Grant 743217 Soft Micro Robotics (SOMBOT). This work was partially funded by BRIDGE through grant number 180861. The authors would like to thank Nanoflex Robotics for providing the model used for the untethered experiments. The authors would also like to thank Magnebotix for their help during the untethered experiments. The authors would also like to thank Noah Rothenberger for the preliminary work done on swarm navigation, and Dr. med. vet. Miriam Weisskopf for her support in the animal lab.

Open access funding provided by Eidgenössische Technische Hochschule Zurich.

### Conflict of Interest

Several of the authors are inventors on a related coil-winding patent. Navion is being commercialized by Nanoflex Robotics, some authors have joined the company, and two are co-founders.

### Data Availability Statement

The data that support the findings of this study are available from the corresponding author upon reasonable request.

### Keywords

ABF, electromagnetic navigation systems, in vivo, microrobot, minimally invasive surgery, particle swarm, remote magnetic navigation

Received: October 16, 2023

Revised: April 15, 2024

Published online:

- [1] J. G. Lee, R. R. Raj, N. B. Day, C. W. Shields, *Microrobots for Biomedicine: Unsolved Challenges and Opportunities for Translation*, 2023.
- [2] N. Ashammakhi, S. Ahadian, M. A. Darabi, M. El Tahchi, J. Lee, K. Suthiwanich, A. Sheikhi, M. R. Dokmeci, R. Oklu, A. Khademhosseini, *Minimally Invasive and Regenerative Therapeutics*, 2019.

- [3] S. Chowdhury, W. Jing, D. J. Cappelleri, *J. Micro-Bio Robotics* **2015**, *10*, 1.
- [4] Y. Wang, J. Shen, S. Handschuh-Wang, M. Qiu, S. Du, B. Wang, *Microrobots for Targeted Delivery and Therapy in Digestive System*, **2023**.
- [5] R. Nauber, S. R. Goudou, M. Goeckenjan, M. Bornhäuser, C. Ribeiro, M. Medina-Sánchez, *Nat. Commun.* **2023**, *14*, 1.
- [6] C. K. Schmidt, M. Medina-Sánchez, R. J. Edmondson, O. G. Schmidt, *Engineering microrobots for targeted cancer therapies from a medical perspective*, **2020**.
- [7] D. W. Chakeres, F. De Vocht, in *Progress in Biophysics and Molecular Biology*, vol. 87, ISSN 00796107, **2005**, pp. 255–265.
- [8] R. Scorretti, N. Burais, L. Nicolas, A. Nicolas, *IEEE Trans. Magn.* **2005**, *41*, 1992.
- [9] S. Rotundo, D. Brizi, A. Flori, G. Giovannetti, L. Menichetti, A. Monorchio, *Shaping and Focusing Magnetic Field in the Human Body: State-of-the Art and Promising Technologies*, **2022**.
- [10] G. L. Jiang, Y. H. Guu, C. N. Lu, P. K. Li, H. M. Shen, L. S. Lee, J. A. Yeh, M. T. K. Hou, *IEEE Trans. Magn.* **2010**, *20*, 8.
- [11] B. K. Chaluvadi, K. M. Stewart, A. J. Sperry, H. C. Fu, J. J. Abbott, *IEEE Robotics Automat. Lett.* **2020**, *5*, 2419.
- [12] J. Vyskočil, C. C. Mayorga-Martinez, E. Jablonská, F. Novotný, T. Ruml, M. Pumera, *ACS Nano* **2020**, *14*, 8247.
- [13] H. Li, J. Tan, M. Zhang, *IEEE Trans. Automat. Sci. Eng.* **2009**, *6*, 220.
- [14] W. Chen, X. Fan, M. Sun, H. Xie, *Mechatronics* **2021**, *74*.
- [15] K. Abolfathi, M. R. H. Yazdi, A. K. Hoshier, *IEEE Trans. Nanotechnol.* **2020**, *19*, 849.
- [16] C. Heunis, J. Sikorski, S. Misra, *IEEE Robotics Automat. Mag.* **2018**, *25*, 71.
- [17] V. Vitiello, S. L. Lee, T. P. Cundy, G. Z. Yang, *IEEE Rev. Biomed. Eng.* **2013**, *6*, 111.
- [18] O. M. Omisore, S. Han, J. Xiong, H. Li, Z. Li, L. Wang, *IEEE Trans. Systems, Man, Cybernetics: Systems* **2022**, *52*, 631.
- [19] N. R. Smilowitz, S. Balter, G. Weisz, *Occupational hazards of interventional cardiology*, **2013**.
- [20] R. Chow, L. A. Beaupre, C. J. Rudnisky, D. Otto, M. Clark, *An Original Study Surgeons' Perception of Fluoroscopic Radiation Hazards to Vision*, Technical report, **2013**, [www.amjorthopedics.com](http://www.amjorthopedics.com).
- [21] R. C. Wan, W. W. Chau, C. Y. Tso, N. Tang, S. K. Chow, W. H. Cheung, R. M. Wong, *J. Orthopaed., Trauma Rehab.* **2021**, *28*.
- [22] J. R. Daryoush, A. J. Lancaster, J. J. Frandsen, J. M. Gililland, *J. Arthroplasty* **2022**, *37*, 1464.
- [23] C. M. Stahl, Q. C. Meisinger, M. P. Andre, T. B. Kinney, I. G. Newton, *Radiation risk to the fluoroscopy operator and staff*, **2016**.
- [24] Stereotaxis Inc., *One Hundred Thousand Procedure Milestone Achieved by Stereotaxis' Robotic Technology*, Technical report, Stereotaxis Inc., **2017**, <https://www.globenewswire.com/>.
- [25] Stereotaxis Inc., *Report OTC\_STXS\_2019 - index to annual on form 10-K* (<https://www.annualreports.com/>), Technical report, Stereotaxis Inc., **2019**.
- [26] J. Hwang, S. Jeon, B. Kim, J. y. Kim, C. Jin, A. Yeon, B. J. Yi, C. H. Yoon, H. J. Park, S. Pané, B. J. Nelson, H. Choi, *Adv. Healthcare Mater.* **2022**, *11*, 11.
- [27] M. Zhang, L. Yang, C. Zhang, Z. Yang, L. Zhang, *IEEE Trans. Instrum. Meas.* **2023**, *72*.
- [28] This applies to both tethered and untethered magnetic tools.
- [29] J. J. Abbott, E. Diller, A. J. Petruska, *Robotics, Auton. Systems* **2019**, *19*, 4.
- [30] B. J. Wellman, M. A. Howard III, R. G. Dacey, M. S. Grady, R. C. Ritter, G. T. Gilles, in *Surgical-Assist Systems*, vol. 3262. SPIE, ISSN 0277786X, **1998**, p. 15.
- [31] M. N. Faddis, W. Blume, J. Finney, A. Hall, J. Rauch, J. Sell, K. T. Bae, M. Talcott, B. Lindsay, *Circulation* **2002**, *106*, 2980.
- [32] Q. Boehler, S. Gervasoni, S. L. Charreyron, C. Chautems, B. J. Nelson, *IEEE Trans. Robotics* **2022**.
- [33] A. J. Petruska, B. J. Nelson, *IEEE Trans. Robotics* **2015**, *31*, 714.
- [34] A. J. Petruska, J. Edelmann, B. J. Nelson, *IEEE Trans. Magn.* **2017**.
- [35] G. Chatzipirpiridis, O. Ergeneman, J. Pokki, F. Ullrich, S. Fusco, J. A. Ortega, K. M. Sivaraman, B. J. Nelson, S. Pané, *Adv. Healthcare Mater.* **2015**, *4*, 209.
- [36] The frequency range tested went from 0.1 Hz to 10 Hz (Figure S18).
- [37] P. A. Turski, M. F. Stieghorst, C. M. Strother, A. B. Crummy, R. P. Lieberman, C. A. Mistretta, in *Application of Optical Instrumentation in Medicine X*, vol. 0347, SPIE, **1982**, pp. 294–295.
- [38] S. Demertzis, S. Hurni, M. Stalder, B. Gahl, G. Herrmann, J. Van Den Berg, *J. Anat.* **2010**, *217*, 588.
- [39] F. Setacci, P. Sirignano, G. de Donato, E. Chisci, G. Galzerano, C. Setacci, *HSR proceedings in intensive care & cardiovascular anesthesia* **2009**, *1*, 37.
- [40] D. Windschall, K. Hoekstra, R. Haase, *J. Ultrasound Med.* **2016**, *35*, 1941.
- [41] L. Zarrinkoob, K. Ambarki, A. Wählin, R. Birgander, A. Eklund, J. Malm, *J. Cerebral Blood Flow Metab.* **2015**, *35*, 648.
- [42] G. Toth, R. Cerejo, *Intracranial aneurysms: Review of current science and management*, **2018**, <https://doi.org/10.1177/1358863X18754693>.
- [43] J. Gralla, G. Schroth, L. Remonda, A. Fleischmann, J. Fandino, J. Slotboom, C. Brekenfeld, *AJNR* **2006**, *27*, 1357.
- [44] F. Ongaro, S. Pane, S. Scheggi, S. Misra, *IEEE Trans. Robotics* **2019**, *35*, 174.
- [45] J. Sikorski, I. Dawson, A. Denasi, E. E. G. Hekman, S. Misra, in *IEEE International Conference on Robotics and Automation (ICRA)*, ISBN 9781509046324, **2017**, pp. 3594–3599.
- [46] J. Liu, Q. Wang, H. Wang, Y. Li, X. Hu, J. Cheng, Y. Dai, *IEEE Trans. Appl. Supercond.* **2016**, *26*, 4.
- [47] S. M. Jeon, G. H. Jang, H. C. Choi, S. H. Park, J. O. Park, in *J. Appl. Phys.*, vol. 111, ISSN 00218979, **2012**.
- [48] S. Kim, M. Cho, S. Im, J. Yun, J. Nam, *Sensors* **2022**, *22*, 15.
- [49] S. Kim, S. Bae, W. Lee, G. Jang, *IEEE Trans. Ind. Electron.* **2024**, *71*, 739.
- [50] When only one Navion is in use, it is not possible to push the magnetic structure away from the Navion. This is a limitation resulting from the three electromagnets arrangement used in the system, two Navions would be necessary to address this limitation (Figure S4, Supporting Information).
- [51] Mark R. Harrigan, John P. Deveikis, *Handbook of Cerebrovascular Disease and Neurointerventional Technique*, volume Springer, Springer, New York, **2013**.
- [52] P. Ryan, E. Diller, *IEEE Trans. Robotics* **2017**, *33*, 1398.
- [53] N. Ebrahimi, C. Bi, D. J. Cappelleri, G. Ciuti, A. T. Conn, D. Faivre, N. Habibi, A. Hošovský, V. Iacovacci, I. S. Khalil, V. Magdanz, S. Misra, C. Pawashe, R. Rashidifar, P. E. D. Soto-Rodriguez, Z. Fekete, A. Jafari, *Magnetic Actuation Methods Bio/Soft Robotics*, **2021**.
- [54] K. Lee, K. M. Lee, M. S. Park, B. Lee, D. G. Kwon, C. Y. Chung, *Spine* **2012**, *37*, 1240.
- [55] B. D. Giordano, J. F. Baumhauer, T. L. Morgan, G. R. Rechtine, *SPINE* **2008**, *33*, 1970.
- [56] C.-J. Lin, R. Blanc, F. Clarencon, M. Pötin, L. Spelle, J. Guillemic, J. Moret, *AJNR* **2010**, *31*.
- [57] B. B. Ghoshhajra, R. A. Takx, L. L. Stone, E. E. Girard, E. S. Brilakis, W. L. Lombardi, R. W. Yeh, F. A. Jaffer, *Eur. Radiol.* **2017**, *27*, 2464.
- [58] A. Schwein, P. Chinnadurai, D. J. Shah, A. B. Lumsden, C. F. Bechara, J. Bismuth, *J. Vasc. Surg.* **2017**, *65*, 1440.
- [59] R. Dreyfus, Q. Boehler, C. Chautems, B. Nelson, in *Proc. 14th Hamlyn Symposium on Medical Robotics*, **2022**.
- [60] R. Dreyfus, Q. Boehler, S. L. Lyttle, S. Charreyron, B. J. Nelson, C. Chautems, *Method and system for manipulating a magnetic instrument within a lumen of a body*, **2023**, US Patent App. 17/824,359.

- [61] B. J. Nelson, B. R. Bendok, E. L. Turcotte, H. Hunt Batjer, *Sci. Robotics* **2024**, 9, 87.
- [62] B. J. Nelson, *Nat. Rev. Bioeng.* **2024**.
- [63] R. Dreyfus, Q. Boehler, S. Lyttle, P. Gruber, J. Lussi, C. Chautems, S. Gervasoni, J. Berberat, D. Seibold, N. Ochsenbein-Kölblle, M. Reinehr, M. Weisskopf, L. Remonda, B. J. Nelson, *Science Robotics* **2024**, 9, eadh0298.
- [64] J. Lussi, S. Gervasoni, M. Mattille, R. Dreyfus, Q. Boehler, M. Reinehr, N. Ochsenbein, B. J. Nelson, U. Moehrlen, *Adv. Intelligent Systems* **2022**, 4, 2200182.
- [65] M. Mattille, Q. Boehler, J. Lussi, N. Ochsenbein, U. Moehrlen, B. J. Nelson, *Adv. Sci.* **2024**, 2400980.
- [66] E. Bonnema, D. Studer, A. Parker, S. Pless, P. Torcellini, *Large Hospital 50% Energy Savings: Technical Support Document*, Technical report, **2004**, <http://www.osti.gov/bridge>.
- [67] H. El Fadil, F. Giri, O. El Magueri, F. Z. Chaoui, *Control Eng. Practice* **2009**, 17, 849.
- [68] Z. D. Deng, S. H. Lisanby, A. V. Peterchev, *Clin. Neurophysiol.* **2014**, 125, 1202.
- [69] M. Sowa, L. Majka, *Nonlinear Dyn.* **2020**, 101, 775.
- [70] S. L. Charreyron, Q. Boehler, B. Kim, C. Weibel, C. Chautems, B. J. Nelson, *IEEE Trans. Robotics* **2021**.
- [71] G. Chatzipirpiridis, S. Gervasoni, C. Fischer, O. Ergeneman, E. Pellicer, B. J. Nelson, S. Pané, *Adv. Intelligent Systems* **2019**, 1, 1900069.
- [72] E. S. Wilks, *Industrial polymers handbook: products, processes, applications*, Wiley-VCH, **2001**.
- [73] A. R. Pelton, D. Stöckel, T. W. Duerig, *Mater. Sci. Forum* **2000**, 327, 63.
- [74] J. Ro, A. Baz, *Compos. Eng.* **1995**, 5, 77.
- [75] D. J. McGrath, B. O'Brien, M. Bruzzi, P. E. McHugh, J. *Mechanical Behav. Biomed. Mater.* **2014**, 40, 252.
- [76] Y. Yu, H. Yuk, G. A. Parada, Y. Wu, X. Liu, C. S. Nabzdyk, K. Youcef-Toumi, J. Zang, X. Zhao, *Adv. Mater.* **2019**, 31, 7.
- [77] S. Shinohara, T. Kihara, S. Sakai, M. Matsusaki, M. Akashi, M. Taya, J. Miyake, *J. Biosci. Bioeng.* **2013**, 116, 231.
- [78] Y. Liu, N. E. Vrana, P. A. Cahill, G. B. McGuinness, *J. Biomed. Mater. Res. - Part B Appl. Biomater.* **2009**, 90 B, 492.
- [79] A. Tian, X. Yi, N. Sun, *Application of mesenchymal stem cells combined with nano-polypeptide hydrogel in tissue engineering blood vessel*, **2022**.